



<http://go.asme.org/HPVC>

Vehicle Description Form

(Form 6)

Updated 12/3/13

Human Powered Vehicle Challenge

Competition Location: Gainesville, Florida

Competition Date: May 8-10, 2015

This required document for all teams is to be incorporated in to your Design Report. Please Observe Your Due Dates; see the ASME HPVC for due dates.

Vehicle Description

School name: Rose-Hulman Institute of Technology

Vehicle name: _____

Vehicle number 2

Vehicle configuration

Upright _____ Semi-recumbent

Prone _____ Other (specify) _____

Frame material 4130 Steel

Fairing material(s) Carbon Fiber, Kevlar

Number of wheels 2

Vehicle Dimensions (*please use in, in³, lbf*)

Length in Width in

Height in Wheelbase 38 in

Weight Distribution Front 47 lbf Rear 23 lbf Total Weight 70 lbf

Wheel Size Front in (406) Rear in (406)

Frontal area 822 in²

Steering Front Rear

Braking Front _____ Rear _____ Both

Estimated Cd 0.085

Vehicle history (e.g., has it competed before? where? when?)

At the time of submission, Shannon-igans has not competed. By the competition, it will have competed at ASME HPVC West.

Rose-Hulman Institute of Technology
2015 ASME East Coast HPV Challenge



Presents

Shannon-igans

Vehicle #2

Team Officers

Louis Vaught, President
vaughtlo@rose-hulman.edu
Mitchell Florence, Secretary
florenwm@rose-hulman.edu
Melissa Murray, Vice President
Ben Griffith, Treasurer
Tyler Whitehouse, Public Relations

Team Advisors

Dr. Michael Moorhead
Associate Professor of Mechanical Engineering
moorhead@rose-hulman.edu
Dr. John McSweeney
Assistant Professor of Mathematics
mcsweene@rose-hulman.edu

Team Members

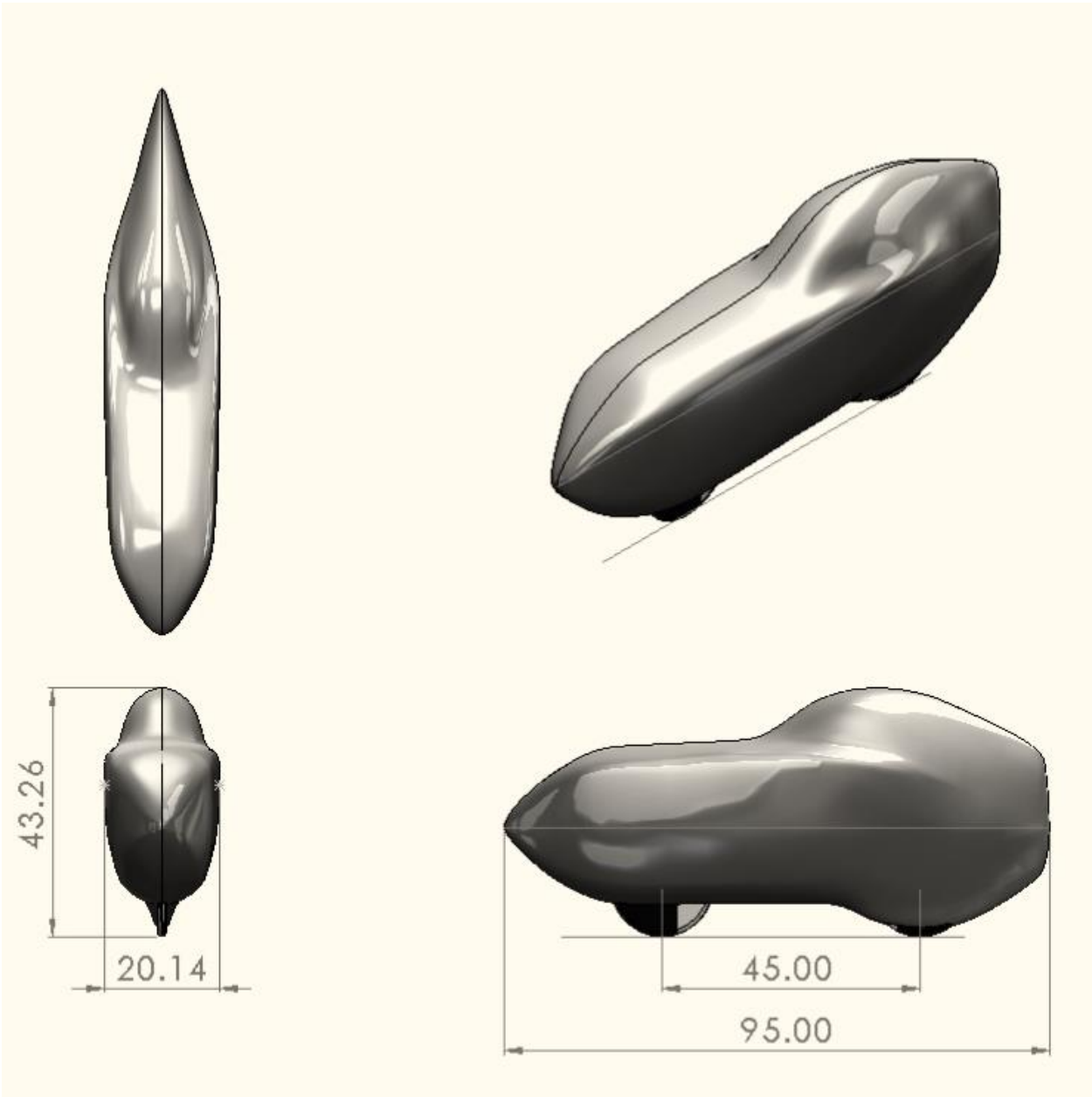
Morgan Bramlette
Luke Brokl
Zeke DeSantis
Jeff Dovalovsky
Dustin George
Ariella Halevi
Alex Hirschfeld

Homa Hariri
Crystal Hurtle
Sabeeh Khan
Will Klausler
Mason Lott
Tianzheng Lu
Tim McDaniel

Drew Miner
David Sampsell
Ben Stevens
Betsy Trainer
Spencer Wright

For more information, visit the team website at: hpvt.rose-hulman.edu

Four-View Drawing



All dimensions shown in inches.

Abstract

During the 2014-2015 competition season, the Rose-Hulman Human Powered Vehicle Team designed and constructed Shannon-igans—a lightweight, efficient, and agile human-powered vehicle that can safely and effectively be used for everyday transportation. The vehicle is a recumbent with a carbon fiber structural fairing and a steel subframes. The fairing weighs 31 lbf (138 N) and was constructed as a continuous structure using a six-piece molding method.

The project's scope included all aspects of vehicle design and fabrication. The team conducted analysis, computational modeling, and physical testing to demonstrate that Shannon-igans met all requirements of Rose-Hulman Institute of Technology, Human Powered Race America events, and the ASME Human Powered Vehicle Challenge.

The team designed Shannon-igans for safety, reliability, practicality, and performance. Standard bicycle components were chosen for the drivetrain and rectangular 4130 steel tubing for the front subframe to increase manufacturability, durability, and reparability. The team designed Shannon-igans with retractable dual landing gear which allows the vehicle to have excellent stability at speeds from 0 to 50 mph. These features combine with a backpack-sized storage space, signal lights, a flag, and a horn to make Shannon-igans a highly practical vehicle.

The vehicle has a field of vision of 200 degrees (300 degrees using mirrors). The faring is protected against penetrating debris using a layer of Kevlar fabric. Both the three-point safety harness and steel roll bar were tested to twice ASME specifications. The team also introduced an innovative all-wheel steering system as well as dual landing gear to improve maneuverability at lower speeds. With robust and novel engineering, Shannon-igans advances the field of human powered vehicles.

Table of Contents

1 Design.....1

1.1	Objective	1
1.2	Background	1
1.3	Prior Work.....	1
1.4	Organizational Timeline	2
1.5	Design Criteria.....	3
1.6	Concept Development and Selection Methods	5
1.7	Bike Description.....	6
1.7.1	Fairing and Frame Design	6
1.7.2	Roll Bar	6
1.7.3	All-Wheel Steer (AWS).....	7
1.7.4	Drivetrain.....	7
1.7.5	Six-Piece Mold.....	7
1.7.6	Landing Gear	8
1.8	Practicality.....	9
1.8.1	Storage.....	9
1.8.2	Weather Conditions	9
1.8.3	Communication	9

2 Analysis.....9

2.1	Rollover Protection System	9
2.2	Structural Analysis	11
2.2.1	Frame Analysis.....	11
2.2.2	Rear Fork Analysis	12
2.3	Aerodynamic Analysis	14
2.4	Cost Analysis.....	15
2.5	Other Analysis.....	17
2.5.1	Gearing	17
2.5.2	All-Wheel Steer	17

3 Testing.....18

3.1	RPS Testing.....	18
3.2	Developmental Testing.....	19
3.2.1	Prone Development Testing	19
3.2.2	Foot Flaps Testing	20
3.2.3	K.I.N.G.E.N. Testing	20
3.2.4	Rib Modification Testing.....	21

3.2.5	Pneumatic Landing Gear Testing	23
3.2.6	Motion Capture.....	23
3.2.7	Layup Testing.....	24
3.3	Performance Testing.....	25
3.3.1	HPVC Obstacle Testing	25
3.3.2	Rear Wheel Turning Radius Testing	25
3.3.3	All-Wheel Steer Durability Testing.....	26
3.3.4	Coastdown Testing	27

4 Safety.....27

4.1	Design Safety.	27
4.1.1	Roll Bar	27
4.1.2	Steering System	27
4.1.3	Seat Belt	28
4.1.4	Windshield.....	28
4.1.5	Safety of Manufacturing.....	28
4.2	Hazard Analysis.....	28

5 Conclusion29

5.1	Comparison	29
5.2	Evaluation.....	29
5.3	Recommendations	29
5.4	Conclusion.....	29

6 Appendix A: Cost.....33

7 Appendix B: Fork Structural.....35

8 Appendix C: KINGEN42

9 Appendix D: Coastdown 425

1 Design

1.1 Objective

The Rose-Hulman Human Powered Vehicle Team (HPVT) designed, tested, and constructed Shannon-igans during the 2014-2015 academic year guided by the team's mission statement:

The Rose-Hulman Human Powered Vehicle Team has the goals of furthering the field of human powered vehicles, creating a common library of knowledge pertaining to their design and construction, developing innovative processes and designs, and providing a positive learning and working environment for students.

The design goal for Shannon-igans was to create an innovative recumbent bike that maximizes speed, stability, and maneuverability for safe personal transportation.

1.2 Background

As energy costs have increased, so too has the demand for sustainable forms of transportation. From 2000-2012, commuter use of unfaired upright bicycles increased nearly 61% from 488,000 to 786,000 commuters [1]. Unfaired upright bicycles are an economical and efficient mode of transportation, but they do not offer the same safety and convenience features as automobiles. Bicycles have low top speeds and offer little in terms of storage space and safety features.

Shannon-igans—a faired, recumbent, all-wheel steered bicycle—captures the practicality and safety features of automobiles while maintaining or improving the efficiency, sustainability, and maneuverability of unfaired upright bicycles. Its design preserves the stability of an upright while achieving the higher possible speeds of a recumbent. A structural, aerodynamic fairing further increases the speed of the vehicle and protects the seat-belted rider better than a normal bicycle. The vehicle boasts sizeable storage space, a seating position designed for maximum rider output, and an electronic rear wheel steer system. These features combine to make Shannon-igans a more practical, efficient, and faster alternative to unfaired upright bicycles.

1.3 Prior Work

The following is a list of features and processes the team developed in previous years that were used in the creation of Shannon-igans.

Wind conditions developed for the CFD analysis of the 2010 Ragnarök were repeated for the fairing design of Shannon-igans [2].

A 3D motion capture processing program, originally developed for the 2011 Helios, was reused to generate a model of the space required inside the vehicle for the rider. This method was used to ensure that the fairing would fit closely around the rider without interfering with the rider's pedal stroke [3].

For its structural fairing, Shannon-igans uses the ribbed tub monocoque concept of the 2012 Carrot Cycle and the 2013 Celeritas. The team has verified this rib layout with the isotropic analysis in ANSYS and orthotropic analysis in Siemens NX performed in 2012 [4].

Structural analysis of the subframe for Shannon-igans has been performed using the loading cases developed for the 2013 Celeritas [5]

The stability of the Shannon-igans was analyzed using a MATLAB program developed for the 2012 Carrot Cycle. The snap-fit method used on the 2012 Carrot Cycle to ensure the hatches were even with the fairing was also used for Shannon-igans [4].

Shannon-igans uses a commercially-fabricated seat belt mounted to the fairing via five steel rivets through an aluminum plate. Using this mounting method, five specimens were tested to failure in 2012. Using Student’s t-test, the 95% confidence interval on the ultimate strength was 810 ± 100 lbf (3600 ± 400 N) [4]. Shannon-igans has three mounts giving 1100 lbf (4900 N) in ultimate strength, exceeding the 2014 HPVC requirement of 750 lbf (3340 N).

The hatch design of Shannon-igans uses the front and rear hatch design of the 2013 Celeritas, modified for ease of access based on previous experience. Similar to the 2013 Celeritas, the rear hatch of Shannon-igans is attached to the vehicle with magnets with the addition of a secondary mechanical attachment method described in Section 1.8 [5].

1.4 Organizational Timeline

The team created a Gantt chart to plan the development process for Shannon-igans. The Gantt chart, shown in Figure 1. Gantt Chart Summary for 2014-2015 Competition Season, was updated periodically to reflect changes and delays.

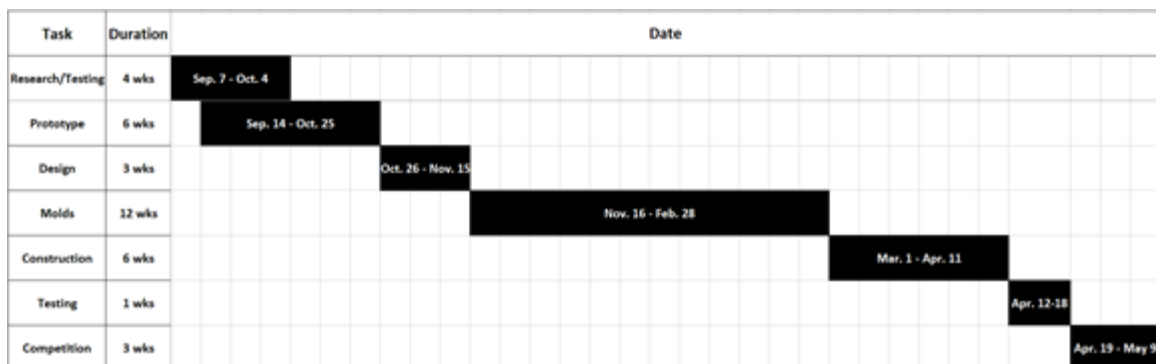


Figure 1. Gantt Chart Summary for 2014-2015 Competition Season

1.5 Design Criteria

The team compiled design constraints for Shannon-igans from ASME HPVC, Rose-Hulman, Indiana state law, and the Human Powered Race America (HPRA) rules and regulations. These constraints are summarized in Table 1. Shannon-igans Design Constraints.

Table 1. Shannon-igans Design Constraints

Source	Constraint
ASME HPVC [6]	<ol style="list-style-type: none"> 1. Cargo area able to hold a 15 x 13 x 8 inch (38 x 33 x 20 cm) parcel 2. Braking from 15 to 0 mph (25 to 0 kph) in less than 20 ft (6.0 m) 3. 26 ft (8.0 m) turning radius 4. Rider safety harness with ultimate tensile strength over 750 lbf (3340 N) 5. Unassisted starts and stops 6. Roll bar with elastic deformation of less than 2 in (5.1 cm) for a 600 lbf (2.67 kN) top load and less than 1.5 in (3.8cm) for a 300 lbf (1.33kN) side load 7. Stability at 3-5 mph for 100 ft (5-8 kph for 30m) 8. Rollover protection system that lessens impact and prevents abrasion in crashes
Rose-Hulman	<ol style="list-style-type: none"> 1. Molds routable out of standard 4 x 8 ft (1.02 x 2.44 m) pieces of foam 2. Total cost of materials and consumables less than \$10,000 3. No exposed carbon fiber near rider 4. Paint scheme comprised of school colors (red, white, and black)
Indiana State Law [7]	<ol style="list-style-type: none"> 1. For riding at night, white front lamp and red rear lamp/reflector visible from 500 ft to front and rear, respectively 2. Bell or other device audible from 100 ft (30 m)
HPRA [8]	<ol style="list-style-type: none"> 1. Two independent braking systems 2. Rear-view mirrors

The team's goals are similar from year to year, but vary based on feedback from previous vehicles, changing requirements, and the innovation that the team implements. Using previous years' experience and the design of Shannon-igans, the team prioritized and matched its needs for the bike with metrics in a House of Quality (HoQ), shown in Figure 2. Shannon-igans House of Quality

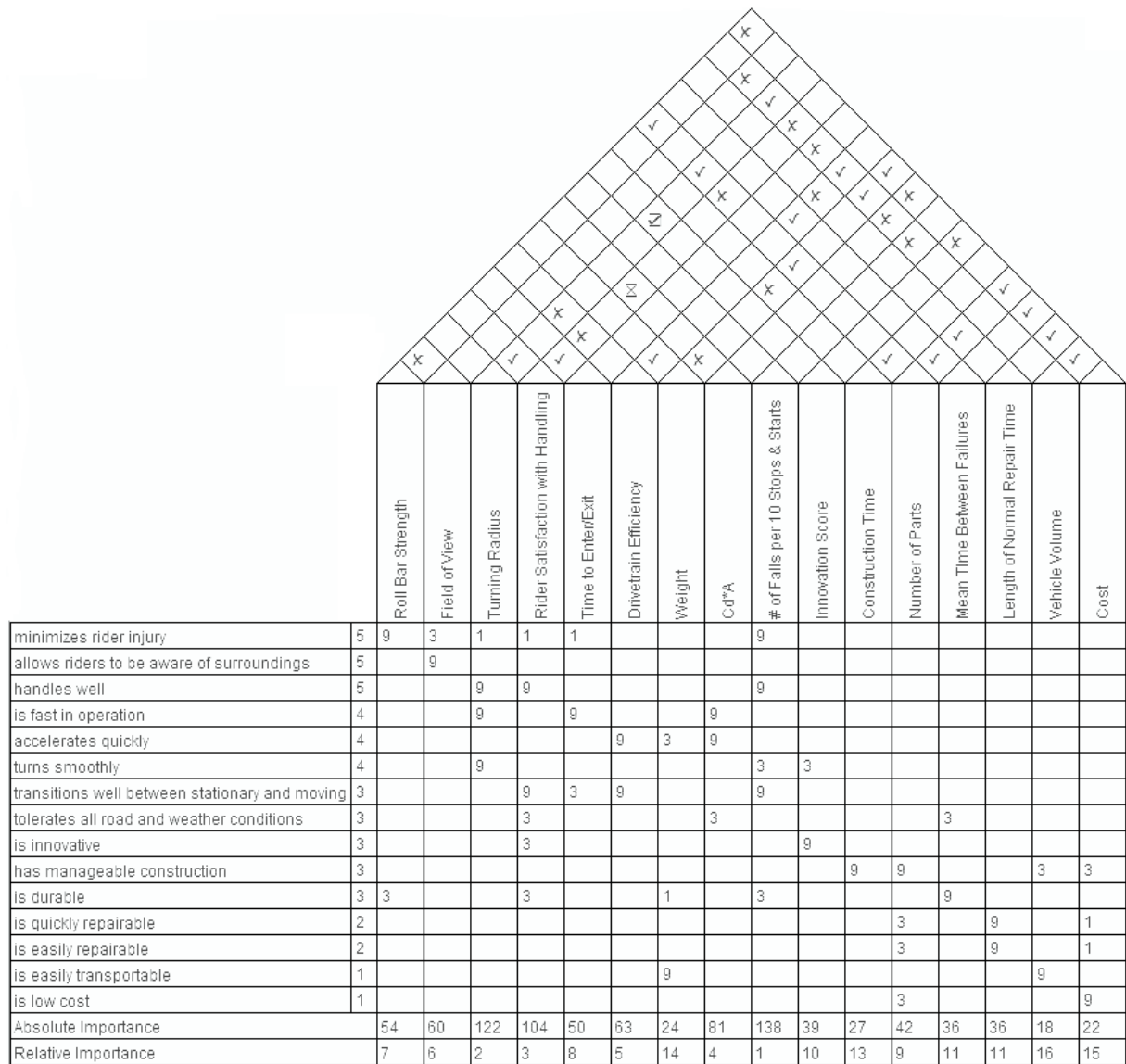


Figure 2. Shannon-igans House of Quality

As shown by the HoQ in Figure 2 above, the areas of focus are turning radius, rider satisfaction, frontal cross-sectional area, and starting-stopping capabilities. From the HoQ, the team developed product design specifications (PDS) to guide the design of Shannon-igans. The PDS are shown in Table 2.

Table 2. PDS Produced from House of Quality

Metric	Marginal value	Target value
falls in 10 stops and starts	1	0
CA (ft ²)	1.2	0.6
part count	100	80
drivetrain efficiency (%)	90	98
rider satisfaction (1-10 scale)	7	10
field of view (deg)	180	360
time to enter/exit (s)	15	3
turning radius (constraint) (ft)	14	6
weight (lbf)	80	50
construction time (weeks)	7	5
cost (excluding labor) (\$)	7,000	5,000

1.6 Concept Development and Selection Methods

Based on the design criteria imposed by the competition and Rose-Hulman, the team developed features for Shannon-igans' design in a decision matrix. The features such as speed and comfort were weighted on a scale of 1 to 5 (1 being least important and 5 being the most important) based on what the team considered most significant to consider when designing the vehicle. Categories considered included vehicle design, low-speed stability methods, seat design, innovation feature, aerodynamic fairing design, storage space location, adjustability method, and layup method. Shown below are some of the design criteria that were taken into account when designing the vehicle.

Selection Criteria	Weight	Recumbent	Tadpole (Recumbent)	Delta	Prone
Speed	5	4	2	1	5
Low Speed Stability	5	3	5	4	2
Rider Comfort	4	4	5	4	1
Maneuverability	4	4	5	3	2
High Speed Stability	4	5	2	3	4
Prior Knowledge	3	5	3	4	1
Weight	3	4	3	2	5
Cost	1	5	3	3	4
Total Score		119	104	86	85

Figure 3. Picture of Vehicle Type Decision Matrix

Innovation Feature	Weight	Rear Wheel Steer	Ability to legally tow	Adjustable mirrors	Gyroscope	Crumple Zone	Electronic Foot Flaps
Innovativeness	5	3	3	3	5	3	2
Feasibility	5	5	3	3	2	2	3
Usefulness	3	5	3	1	5	1	3
Reliability	3	4	5	3	3	5	2
Cost	3	3	4	5	1	5	4
Bonus Points	2	1	1	5	1	1	1
Total Score		78	68	67	64	60	54

Figure 4. Picture of Innovation Feature Decision Matrix

Values for the decision matrix were generated by the consensus of the team using prior experience or ongoing testing. The decision matrix indicated the recumbent bicycle as the preferred vehicle layout and an All-Wheel Steer system as the preferred innovation feature. Decisions regarding all other possible aspects of the vehicle are discussed further in the remainder of the report.

1.7 Bike Description

1.7.1 Fairing and Frame Design

To implement a steering rear wheel, the team had to redevelop the portions of the monocoque fairing which depended on integrating the rear wheel mount to the fairing structure. The rear wheel of Shannon-igans is now mounted directly to the roll bar, just behind the rider. This structure also acts as a cross member for the roll bar contributing to its lateral stiffness.

Rib placement throughout the vehicle was also designed to minimize deflection and maximize stiffness between the pedals and the rider, and to allow the rider space to move. The ribs are constructed of unidirectional carbon fiber wrapped around Nomex honeycomb. The ribs are laid up within the carbon fairing forming one strong structural member throughout the vehicle. Additionally, Shannon-igans has a separately constructed subframe to support the front wheel, steering mechanisms, cranks, and drivetrain attached at structural points in the fairing/frame.

The fairing has four hatches that can be used or detached. The main hatch comprises the majority of the top half of the fairing and acts as the main point for entering and exiting the vehicle. Two small side hatches in the upper portion of the tailbox provide access to electronics and pneumatic systems mounted behind the rider. The most unique hatch on Shannon-igans is the rear-wheel cowl. This covering for the rear wheel decreases aerodynamic drag and also significantly reduces the turning angles of the rear wheel. The use of the rear cowl depends on the rider's intentions when beginning the ride. When maneuverability is key the rear cowl can be removed; for long straight rides the rear cowl can be left on to conserve the rider's energy and extend his or her range.

1.7.2 Roll Bar

Shannon-igans uses an integrated roll bar to protect its rider. It consists of a 2.50 in (63.5 mm) x 0.25 in (6.35 mm) strip of Nomex honeycomb wrapped with multiple layers of unidirectional and woven carbon fiber. The order of the layers is shown in the following diagram.

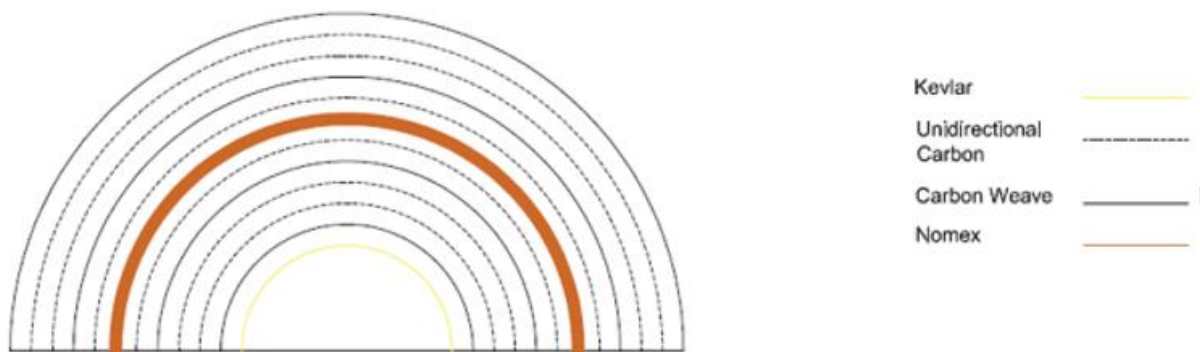


Figure 5. Roll Bar Layers

1.7.3 All-Wheel Steer (AWS)

The All-Wheel Steer (AWS) system on Shannon-igans centers around a rear mounted fork as shown in Figure 6. This fork is structured much like the fork at the front of a normal bicycle, but faces in the opposite direction. The headtube for the fork is constructed as part of a rear subframe assembly, which attaches to the roll bar rib on either side of the vehicle, directly behind the rider. The fork is actuated by a 1271 oz-in (1.418 kg-mm) servo motor, which is connected to the fork by a chain and sprockets. The rider is able to control the angle of the rear wheel independently of the front wheel with a joystick mounted on the steering tiller. Allowing for the front and rear wheels to steer independently allows for greater maneuverability than is possible with a fixed rear wheel or a rear wheel rigidly linked to the position of the front wheel.



Figure 6: All-Wheel Steer Prototype

1.7.4 Drivetrain

Drawing from experience with the 2014 Namazu, the team designed Shannon-igans with a narrow-Q factor drivetrain. The 2014 Namazu required a drivetrain with sufficient clearance between the pedals for a stored energy drive system [9], which significantly increased the frontal area of the vehicle and caused chain interference while turning due to decreased clearance between the two drive chains. The 2013 Celeritas was designed with a narrow-Q drivetrain and had no issues with chain interference, thus this system was redesigned for use on Shannon-igans. From research on similar systems, the team concluded that it met its PDS value of 95% on drivetrain efficiency [10].

1.7.5 Six-Piece Mold

The team used a Six-Piece Mold procedure in the production of the Shannon-igans, refined from its original application for the 2013 Celeritas. The vehicle was created in four separate layups, visualized in Figure 7 clockwise from top left: top and side hatches, two-thirds of the monocoque, foot flaps and rear-wheel cowl, and bottom two-thirds of the monocoque. Both the 2013 Celeritas and 2014 Namazu layups experienced problems drawing adequate vacuum for the larger monocoque layups due to the complex contours of the fairing. Both vehicles used a large wooden box that supported and aligned the mold pieces during the layup and while under vacuum. This box was difficult to fit inside a vacuum bag and could not be vacuum sealed, resulting in unreliable vacuums.

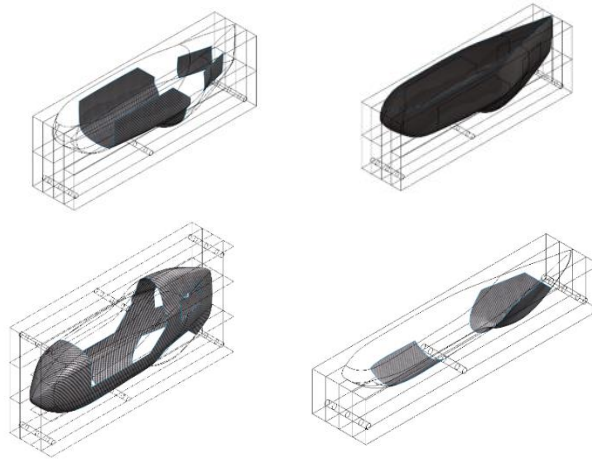


Figure 7. Layup Order of the 6-Piece Mold Process, Clockwise from Top Left

As discussed in Section 3.2.7, the team successfully tested and implemented a layup process without a box. To align the mold pieces, the top and bottom thirds had three holes routed that snugly fit aluminum alignment rods. Each of the six pieces of the mold was hardened with EPSILON Impact Resistant Foam Coating to prevent damage from the rods and provide a finished surface. For additional rigidity, each mold piece was backed with half-inch plywood. The rods and plywood created a rigid, adjustable structure without the alignment box. This change produced several unexpected benefits: significantly quicker layup preparation in comparison to the 2014 Namazu, easier access to the molds during layups due to removal of the bulky box, and significantly higher vacuum pressures than were seen in the production of the 2013 Celeritas and the 2014 Namazu.

1.7.6 Landing Gear

The last landing gear designed by the team, for the 2013 Celeritas [5], used a locking mechanism and a motor to extend and retract a telescoping rod. The mechanisms required to perform this resulted in a complicated and heavy system. Though it was functional, the landing gear supported the vehicle on only one side, which required practice to use successfully. This year, the team's goal was to design a system that supported both sides of the vehicle while weighing less and actuating more quickly. Pneumatic actuation was chosen for its high energy density and flow rate, ease of construction, and ability to power two mechanisms simultaneously. The pneumatic piston actuator is eight pounds (3.63 kg) lighter than the old actuation mechanism. After adding a second piston, piston supports, a tank, a regulator and an electric solenoid, the system weighs one pound (0.454 kg) less than the previous single-sided electric system.

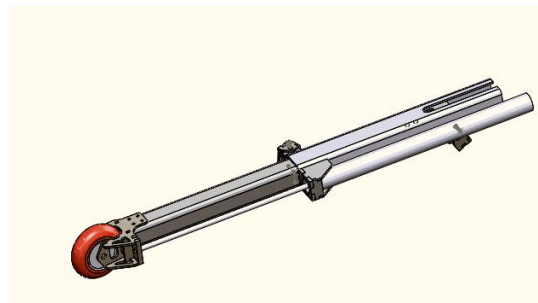


Figure 8. Single Side of Landing Gear Design

1.8 Practicality

The team designed Shannon-igans so that it could be both a HPVC racing vehicle and a practical means of personal transportation. In its construction, standard bicycle components were used wherever possible for ease of replacement. The composite fairing is durable, protects the rider during crashes, and can be repaired to useable strength as seen in Section 3.2.4. With its improved landing gear and rear wheel steer systems, Shannon-igans achieves stability and gives the rider the ability to easily stop and start the vehicle unassisted.

1.8.1 Storage

The cavity directly behind the rider is used for storage, as with prior vehicles such as the 2014 Namazu. The storage space is easily accessible through the rear hatch and measures greater than 15 x 13 x 8 inches (38 x 33 x 20 cm).

1.8.2 Weather Conditions

Shannon-igans is suitable for the rider to travel in a variety of weather conditions. The team determined temperatures from 15°F (-9°C) to 95°F (35°C) to be reasonable conditions for riding. This range extends above 80°F (27°C) because of an included air duct and exit, which efficiently ventilate the rider while riding, and extends below 32°F (0°C) due to the insulating properties of the fairing if the exit hole is sealed. Because of this range, Shannon-igans is rideable in most of the continental United States, in particular the 2015 HPVC locations of Gainesville, FL and San Jose, CA. The fairing provides significant protection from precipitation but is it not advised to ride when there is rainwater or snow on the road, as the wheels are in the rider compartment, and may splash liquid at the rider.

1.8.3 Communication

Shannon-igans has a headlight, turn signals, brake lights, and horn that allow the rider to interact with motorists, pedestrians, and other cyclists' safely. The headlights are visible at night from over 500 ft (150m) and the horn is audible from over 100 ft (30 m). These meet the constraints imposed by Indiana state law (shown in Table 1). Additionally, Shannon-igans is equipped with a two-way radio during competition to allow the rider to communicate with team members.

2 Analysis

2.1 Rollover Protection System

Objective	Method	Results
Verify the strength of the rollover protection system keeping the rider safe	ANSYS Structural was to determine deflection in two load cases	The roll bar meets ASME specification with a top load deflection of 0.40 in (10.2 mm) and a side load deflection of 0.27 in (6.9 mm)

The analysis of the roll bar was performed using Finite Element Analysis (FEA). To simplify the calculations the nomex core was modeled as an isotropic material with material properties matching 3 lb (13.3 kg) polyurethane expanding foam. Bending tests performed for the 2012 Carnot Cycle indicated that the material internal to the rib primarily provides support against buckling [4]. The carbon fiber weave and uni-directional carbon fiber were modeled as orthotropic materials with values

gathered from experimental data [5], calculations from material spec sheets, and material properties from the team's distributors [11][12]. Additionally, the roll bar was modeled without the steel support beam. During the analysis, the bottom of the roll bar was treated as a fixed location as a close approximation since the steel bar will deflect minimally. The calculated material properties can be seen in the Table 3. With a top load of 600 pounds of force (2669 N) applied to the roll bar, the deflection was calculated to be 0.40 inches (10.2 mm). With a side load of 300 pounds of force (1334 N) the calculated deflection was 0.27 inches (6.86 mm). Both of these values can be seen in Figures 9 and 10 and fall well within ASME specifications for the 2015 HPVC [6], assuring the team that the design and rib structure was adequate. Additionally, the team expects the final roll bar produced to be significantly stronger due to the nature of the monocoque design. Due to the complex nature of FEA, the team verified the reliability of the result by modeling a rib in three-point bending. This is a common test the team has used to test the effects of processes like rib repairs and rib pinning. Since this data was readily available, the team modeled one of these ribs and did analysis with the average failure force of 150 pounds (667 N). The modeled rib reported a maximum strain of 0.03 which falls just over the reported expected failure of carbon weave by itself.

Table 3. Material Properties used in Finite Element Analysis of the Rollbar and Rib Crush

	UD Carbon			Carbon Weave			Nomex		
Property	Value		Value		Property	Value			
Density	1.6	g cm ⁻³	1.6	g cm ⁻³	Isotropic Elasticity				
Orthotropic Elasticity					Derive from	Young's ...			
Young's Modulus X direction	1.35E+11	Pa	7E+10	Pa	Young's Modulus	1E+05	Pa		
Young's Modulus Y direction	1E+10	Pa	7E+10	Pa	Poisson's Ratio	0.3			
Young's Modulus Z direction	3.4474E+09	Pa	3.4474E+09	Pa	Bulk Modulus	83333	Pa		
Poisson's Ratio XY	0.3		0.3		Shear Modulus	38462	Pa		
Poisson's Ratio YZ	0.3		0.3						
Poisson's Ratio XZ	0.3		0.3						
Shear Modulus XY	5E+09	Pa	5E+09	Pa					
Shear Modulus YZ	2.5E+08	Pa	2.5E+08	Pa					
Shear Modulus XZ	2.5E+08	Pa	2.5E+08	Pa					

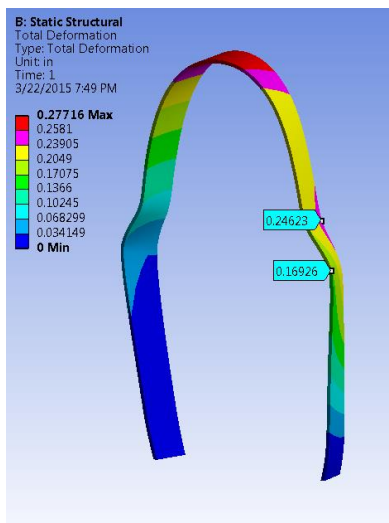


Figure 9. Roll Bar with Side Load

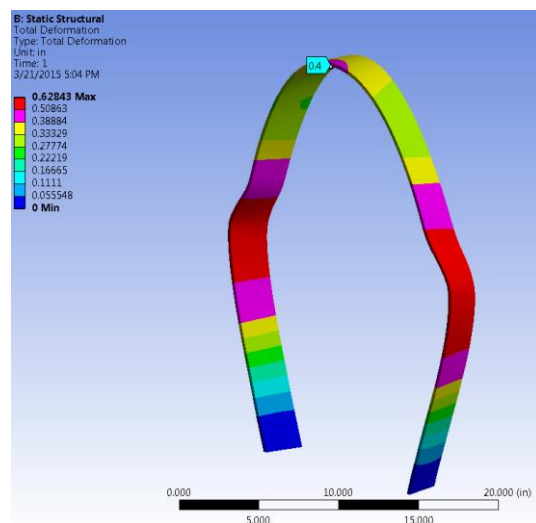


Figure 10. Roll Bar with Top Load

2.2 Structural Analysis

2.2.1 Frame Analysis

Objective	Method	Results
Determine the amount of material necessary to support the loads on the steel sub-frame with a factor of safety of 6.	FEA was performed on the subframe design using team standard loading conditions.	Rectangular 1 x 1 ½ inch steel tubing with a wall thickness of 0.065 inch is sufficiently strong for the subframe

The team simulated the stress in the subframe with FEA, using ANSYS. To simulate the rider's pedaling, a moment of 19 lbf-ft (26 N-m) and a force of 173.33 lbf (771.3 N) were applied to the bottom bracket. A force of 127 lbf (565.2 N) was applied to the head tube to simulate the weight distribution of the rider. These loadings were originally developed for design of the 2013 Celeritas [5]. The worst situation, in which only the edge of the mounting plates are in contact, was simulated. The result shows that the main part of the subframe has a high factor of safety (FoS) and the FoS for several moderate stress concentration locations stay over 10. The most severe stress concentrations happen around the edge of the rear mounting slot and inner surface of the bottom bracket. On the edge of rear mounting slot, the maximum stress is 13 ksi and the FoS for yielding is 5.75; the stress on the bottom of inner side of bracket is around 9 ksi and the FoS for yielding is 8.31. The team has a target FoS of 6 to ensure that this critical system does not fail. Although the minimum calculated FoS of 5.75 is below this target, the team feels that it is still within a reasonable range, and the design is adequate.

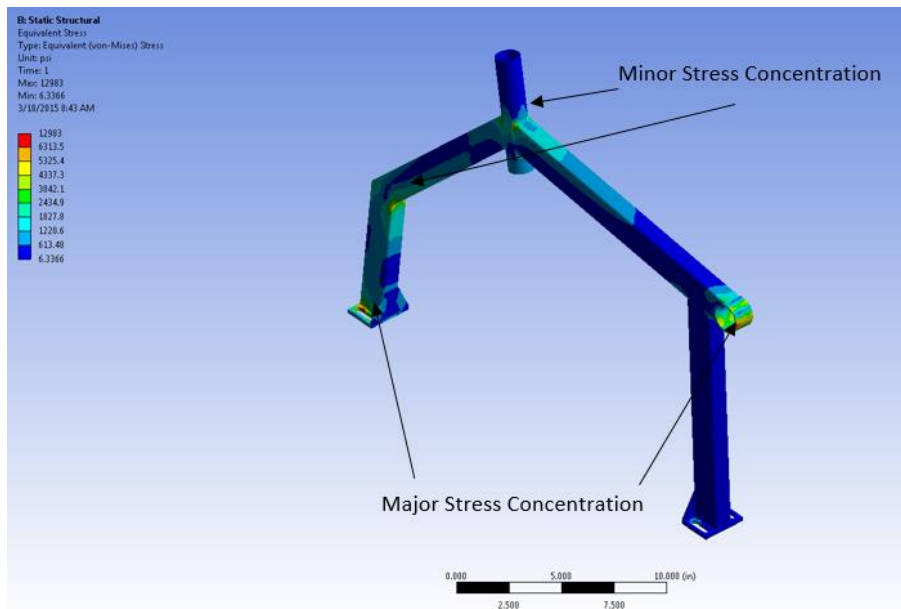


Figure 11. Stress Concentrations on Frame

2.2.2 Rear Fork Analysis

Objective	Method	Results
Design a fork for the all-wheel steer system that fulfills all geometry requirements and ASTM strength requirements.	Two FEA solvers were used to perform both iterative design of the fork and validation analysis.	The final design for the rear fork met all requirements as well as being significantly lighter weight than those produced in the past

Shannon-igans required construction of a rear fork for use in the rear-wheel steer system. The system was designed with a zero-trail condition to ensure that in the event of system failure, the rear wheel would remain straight. Since the 2007 Infinity, the team has constructed forks by modifying commercial bicycle forks. However, this method is too imprecise to yield a zero-trail condition. Instead, a custom fork was designed and CNC-milled to specification.

For design purposes, the loading conditions chosen were those set forward by ASTM F2273-11. The specification requires a fork to withstand a compression load of 2800 N (639 lbf) parallel to the steer tube, and a bending load of 1200 N (270 lbf) perpendicular to the steer tube against the rake of the fork. These loads are to be applied through the wheel dropouts while holding the steer tube fixed using thrust bearings. As standard bicycle forks are subject to increased loading during braking as well as frontal impact loading, this specification was chosen to guarantee a robust design.

To determine if the fork was of adequate strength, von Mises stress plots under loading were analyzed for material exceeding yield strength. The fork was designed to be CNC milled from 7075-T6 aluminum billet, and so was analyzed using a yield strength of 505 MPa and a modulus of elasticity of 71.7 GPa.

To simplify this analysis, a symmetry argument was used to reduce the fork by cutting along the Y-Z plane and analyzing half of the model. A zero-displacement boundary condition was defined along the X-axis, which is perpendicular to the cutting plane. Each of the loads applied to the fork were halved and applied to the wheel dropout. A preliminary SolidWorks simulation was performed to determine the adequacy of the design. A fixed support case was applied to the outer surface of the steer tube and to the surface along the axis of symmetry. A 1400 N axial force and a 600 N bending force were applied to the wheel dropouts in turn. The following von Mises stress plots were produced:

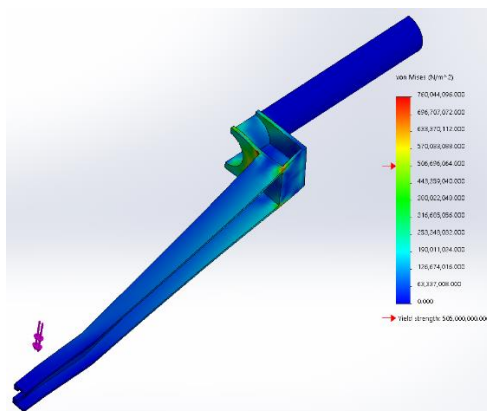


Figure 12. Preliminary Bending Case von Mises Stress

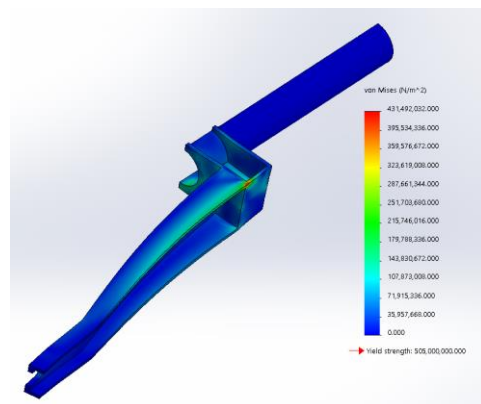


Figure 13. Preliminary Axial Case von Mises Stress

From this analysis, it was determined that the crown of the fork significantly exceeded von Mises yield stress for the bending case. The design was modified to stiffen the crown by adding a diagonal brace from the fork blade to the steer tube. The following simplified final design was produced for analysis:

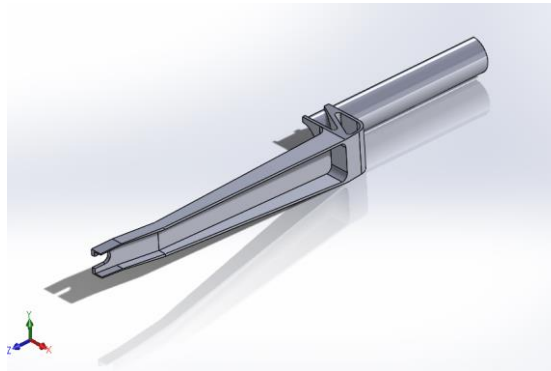


Figure 14. Simplified Final Fork Model

Two separate methods of analysis were used for comparison: SolidWorks SimulationXpress Wizard and ANSYS Workbench 14.0 Static Structural Solver. The SolidWorks simulation was performed as accurately as possible given the constraints set forth by the solver. A fixed support case was applied to the outer surface of the steer tube and to the surface along the axis of symmetry. A 1400 N (315 lbf) axial force and a 600 N (135 lbf) bending force were applied to the wheel dropouts in turn, and the fork was analyzed for maximum von Mises stress and maximum total deflection in each loading case.

The ANSYS Workbench simulation was performed using a fixed support case applied to the crown race of the fork. The top of the fork was fixed against Z-displacement to mimic the thrust bearing assembly of a headset. Finally, the face of the fork along the axis of symmetry was fixed against x-displacement. A 1400 N (315 lbf) axial force and a 600 N (135 lbf) bending force were applied to the wheel dropouts in turn, and the fork was analyzed for maximum von Mises stress and maximum total deflection in each loading case.

Shown below in Table 4 is a summary of the relevant maximum von Mises stress and maximum total deflection obtained from both axial and bending loads for each analysis. The SolidWorks and ANSYS analyses agree that the fork will not fail under the design loading conditions. Detailed reports of the solutions obtained are included in Appendix B.

Table 4. Summary of Results from Both Analysis Methods

Analysis	Axial von Mises (MPa)	Axial Total Deflection (m)	Bending von Mises (MPa)	Bending Total Deflection (m)
SolidWorks SimulationXpress	130	0.00513	443	0.00580
ANSYS Workbench	140	0.00452	430	0.00957

2.3 Aerodynamic Analysis

Objective	Method	Results
Determine the fairing shape to make Shannon-igans easiest to pedal	A 2d trade study of various fairing shapes was performed. ANSYS Fluent CFD analysis was performed iteratively.	At 45.5 mph, Shannon-igans fairing will see a 1.55 lbf (6.89 N) drag force. In a 13.6 mph cross wind, Shannon-igans fairing will experience a 20.5 lbf (91.1 N) lateral force.

Aerodynamic analysis is involved in choosing the vehicle type, the designing of the fairing, and cooling the rider. It is critical for the vehicle to have a low drag force at endurance paced speeds (20-30 mph) and sprinting speeds (40+ mph). It was determined based on preliminary 2-dimensional CFD analysis that a prone vehicle would be the most aerodynamic, followed closely by recumbent, then trike as shown in Table 5.

Table 5. Cd Analysis of Bike Types

	Prone	Recumbent	Tricycle
Cd	0.0839	0.103	0.217

A prone would allow for a slightly smaller frontal area than a recumbent and also promotes a more streamlined teardrop shape for the fairing, since the rider's shoulders define the widest point and a prone puts the shoulders closer to the nose of the vehicle than a recumbent does. A trike must have either two wheels outside the main body of the vehicle, or an increased frontal area of the fairing to fully enclose all wheels. Although a prone has the potential to be more aerodynamic than the recumbent, other factors such as rider comfort and previous experience developing prones drove the team to choose a recumbent bicycle design.

The fairing was designed around the set of curves which outlined the riding motions of variously-sized riders. The curves were generated by Motion Capture Software using the processes described in Section 3.2.6. An initial design was generated based on optimizing rider space and minimizing disturbance to the airflow around the vehicle. The design was iterated upon through the use of computational fluid dynamics (CFD). The CFD of the 2015 Shannon-igans was performed using Fluent in ANSYS Workbench. SolidWorks Flow Simulation was used to calculate the CFD of the 2014 Namazu, but the team found ANSYS Fluent possesses more CFD capabilities. Simulations were done on a symmetrical half bike model for the case of airflow parallel to the direction of the vehicle and on a full bike model for the case of a cross wind. The focus of these iterations was to minimize flow separation on the rear half of the fairing and thus reduce pressure drag. Because of the limitations on the length of the fairing due to both weight optimization and mold fabrication, flow separation could not be fully eradicated.

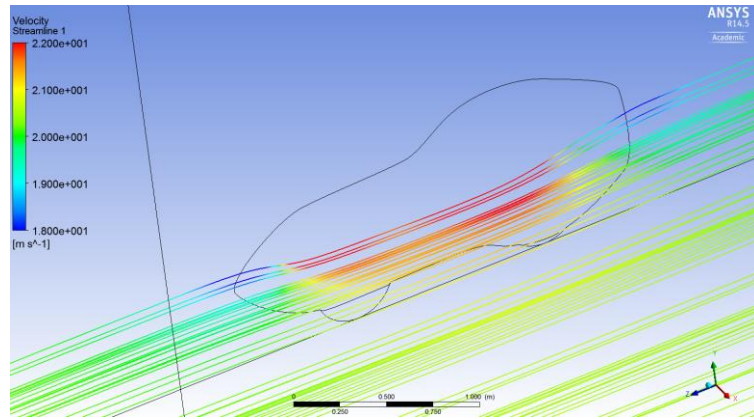


Figure 15. Aerodynamic Analysis using ANSYS

Table 6. Drag Force of Shannon-igans Compared to Previous Vehicles

Fairing Shape	Force at 45.5 mph (lbf)	Lateral Force with 13.6 mph	Bike width at shoulders (in)
Shannon-igans	1.52	23.4	19.8
Namaz	1.55	20.5	19.7
Celeritas (2013)	1.47	26.6	18.4
Carnot Cycle (2012)	1.66	24.6	19.8

In previous years' vehicles, the rider was cooled by the airflow drawn in through a NACA duct on the top hatch. A NACA duct is specifically designed to take in the free moving fluid over the surface of a body by creating vortices that allow the duct to capture the free stream fluid. This decreases in drag compared to the amount of airflow drawn in. In past years, the team has struggled with overheating riders which frequently causes riders to compete in the endurance race without the top hatch on, thus removing the benefit of the fairing. The lack of effectiveness of the NACA duct was due to both the small size used and the lack of a designed outlet for the internal airflow. This means that the air was forced to exit at the relatively high pressure zone at the front wheel opening, or through any other small openings in the body of the vehicle. To fix this problem, an outlet was added to the tail of the vehicle. The low pressure zone at the rear of the vehicle will help draw out air from inside the bike and increase the cooling experienced by the rider. Furthermore, the overall size of the NACA duct was increased by 50% to increase airflow further.

2.4 Cost Analysis

Objective	Method	Results
Determine the cost of producing Shannon-igans and the cost of a three year production run	Created a financial account of parts, materials, overhead, labor, tooling, and capital investment	Shannon-igans cost \$15,141 to produce (including labor), but would cost \$9,259 per vehicle in a production run

The cost to produce Shannon-igans and a 3 year, 5 vehicle/month production run are shown below.

Table 7. Cost Breakdown of Major Vehicle Components

Section	Materials	Skilled Labor Hours	Materials + Labor Costs
Drivetrain	\$1,504.00	10	\$1,704.00
Fairing	\$1,897.00	70	\$3,297.00
Subframe	\$117.00	10	\$317.00
Rear Wheel Steer	\$427.00	35	\$1,127.00
Electronics	\$50.00	15	\$350.00
Safety/Comfort Features	\$100.00	12	\$340.00
Molds	\$806.00	360	\$8,006.00
Total for One Vehicle	\$4,901.00	512	\$15,141.00

Table 8. Cost Breakdown of Major Vehicle Components

Material Costs for 180 Vehicles	\$627,341.00
Labor Costs for 180 Vehicles	\$417,600.00
Overhead Costs for 180 Vehicles	\$544,640.00
Tooling Costs for 180 Vehicles	\$22,972.92
Capital Investment for 180 Vehicles	\$54,000.00
Total Costs	\$1,666,553.92
Cost Per Vehicle	\$9,258.63

The cost of materials for Shannon-igans includes both costs incurred by the team and estimates for donated goods. The material costs total \$4,901, which fell beneath the PDS marginal value of \$7,000. Man hour estimates were obtained from the project schedule, and an assumed average hourly wage of \$20 to obtain labor costs for the vehicle as-presented.

When scaling up production to 180 vehicles over three years, some costs are reduced and new ones are added. Labor and material costs were estimated to decrease by 25% and 15% respectively, due to process optimization and bulk-volume purchasing associated with a production system. New costs include capital, tooling, and overhead. Capital costs include heavy machinery, workspace/warehouse leasing, and all tools that last the duration of the production. Tooling costs include the price of tools needing replacement either after every build or periodically during production. Overhead costs include office space rental, insurance, and additional staff. Molds were treated as a one-time cost for materials and labor, as they were considered to be durable enough to reuse. Itemized production costs are given in Appendix A.

The cost for the vehicle as-presented is \$15,141. The estimated cost per vehicle for a production run is \$9,258. The largest contributing factor to the price reduction is the re-use of the mold, which represents 53% of the total cost of the prototype as-presented. This production cost is significantly higher than the only marketed fully-faired vehicle, the Lightning F-40, which retails for \$6,100 [13]. The team considers this cost acceptable due to the increased safety of a full carbon fiber fairing as well as the unique independent all wheel steering system.

2.5 Other Analysis

2.5.1 Gearing

Objective	Method	Results
To determine gear ratios for competition	Vehicle velocity was related to pedal speed. Mid-drive gain ratio was modified to achieve the desired speed range.	A mid-drive gain ratio of 14:22 was found to yield the optimal speed range of 8-50 mph (11-85 kph).

The team selected gear ranges according to a comfortable cadence range of 60-120 RPM and the speeds observed in previous HPVC races. The maximum and minimum sustained speeds for the 2014 races were 36 mph (58 kph) during the sprint event and 5 mph (8 kph) in the endurance event. By a proper range of gears, Shannon-igans achieves these speeds at the appropriate cadences.

The team used an 18.5 in (47 cm) diameter wheel, a 60 tooth front chainring, and an 11–36 tooth cassette as the basis for the gearing design. From these parameters, a mid-drive gain ratio of 13:17 achieved the target output range. At 60-120 RPM, the rider can maintain speeds between 6 and 46 mph (10 to 74 kph). A rider can maintain a speed less than 6 mph (10 kph) at a cadence below 60 RPM.

2.5.2 All-Wheel Steer

Objective	Method	Results
To explain the separate turning cases seen in all-wheel steering	Dynamical analysis	The turning cases were adequately explained to determine the benefits of all-wheel steering

When a turn is initiated to right with the front wheel of a bicycle, the wheel pulls the front contact patch to the right. This force to the right tilts the bike out of the turn. Coupled with the appropriate fork geometry, this phenomenon helps a front wheel steer bike self-stabilize and be inherently easy to ride. As a moving bike begins to fall to the right, the fork geometry causes the front wheel to turn to the right which in turn causes the bike to tilt back to the left and remain balanced. This is shown in Figure 16.

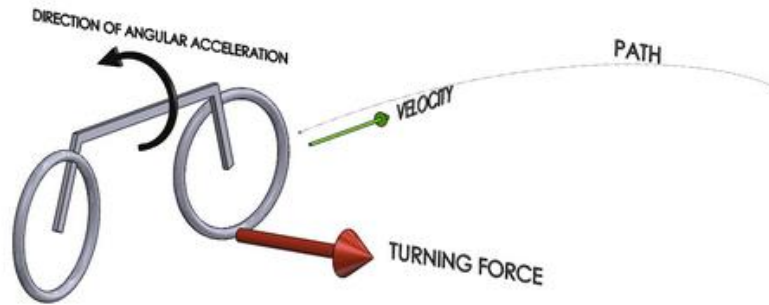


Figure 16. Turning Right with Front Wheel

When a turn is initiated to right with the rear wheel of a bicycle, the wheel pulls the rear contact patch to the left. This force to the left tilts the bike into the turn. In the case of the all-wheel steer bicycle, the benefit of this phenomenon is that the rider does not need to initiate a turn beforehand by countersteering or destabilizing in the direction of the turn, as they would in a strictly front wheel steer bike. Initializing a turn with the rear wheel leans the bike into the turn which promotes dramatically quicker and sharper turning and increased rider confidence. This is shown in Figure 17.

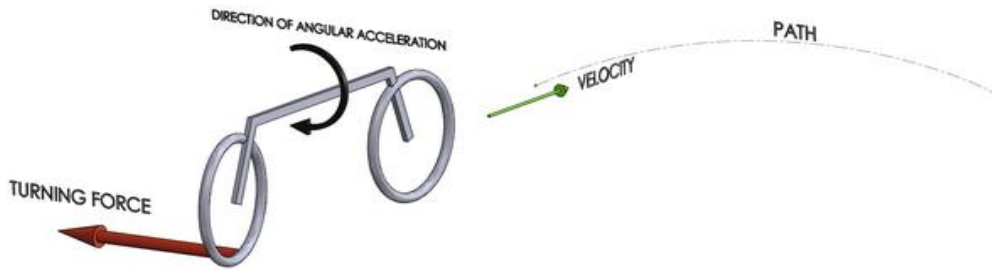


Figure 17. Turning Right with Rear Wheel

3 Testing

3.1 Rollover Protection System Testing

Objective	Method	Results
Determine whether the Shannon-igans roll bar will offer adequate protection in the event the of the vehicle landing on its side or an inverted crash.	Loads were applied to a duplicate of the RPS.	The Shannon-igans RPS exceeds the ASME requirements.

The team conducted compression testing to confirm that the Rollover Protection System (RPS) meets the specifications of the Rules for the 2015 Human Powered Vehicle Challenge [6]. The team made a duplicate RPS using the same materials, geometry, and process as the RPS in Shannon-igans for testing. The RPS was attached to a steel testing rig to approximate the rear subframe assembly, which also served to fix the system in the testing apparatus. The team applied loads as specified in the HPVC Rules to the duplicate RPS and measured the resultant deflection. Results from ANSYS and testing can be found in Table 9.

Table 9. Deformation in the Roll Bar

Elastic Deformation	ANSYS Workbench	Tensile Testing
Top Load—600 lbf (2670 N) at 12° from vertical towards aft	0.4 inch (10.2 mm)	0.3 inch (7.6 mm)
Side Load—299 lbf (1330 N) horizontally at location of shoulder	0.27 inch (6.9 mm)	1.10 inch (27.9 mm)

Negligible permanent deformation (less than 0.07 inch) occurred when the RPS was loaded to HPVC specifications, evidenced by post-test height measurements and the lack of visible or audible indicators during the test. The team also tested the RPS to failure in the top load condition, reaching a maximum load of 940 lbf (4181 N). Afterwards, the roll bar sustained approximately 800 lbf (3559 N) for several more seconds before failing completely. The Shannon-igans RPS system had to sustain a 600 lbf (2670 N) vertical load and a 299 lbf (1330 N) lateral load condition. The Shannon-igans RPS meets and exceeds these load constraints set by ASME for the 2015 HPVC.

3.2 Developmental Testing

3.2.1 Prone Development Testing

Objective	Method	Results
Test the suitability of the prone position for the HPVC	Design and construct a prototype prone frame and rider harness. Test rider fitment and comfort	Riders were uncomfortable with both position and harness method, requires significant further development and testing

In recent years, the HPVC has introduced new requirements to the Endurance and Sprint events that has resulted in significant upheaval of the established designs. The 2014 Namazu was designed as a tilting tricycle in an attempt to meet these new requirements, but the team was dissatisfied with its overall speed and handling. For the 2015 competition, the team desired to compare all reasonable vehicle configurations, including delta tricycle, tadpole tricycle, recumbent bicycle, and prone bicycle. The team had no prior experience with prone vehicles, and so began construction of a prototype.

Vehicle stability was determined using a Matlab program developed from *Lords of the Chainring* by Dr. Patterson of Cal Poly SLO. From this, a wheel spacing of 54 inches (1.37 m) and a headtube angle of 79 degrees were chosen. The fit of the rider was determined by jiggling the front wheel, rear wheel, and pedals and suspending the rider above them using an adjustable table. From this, rider height to clear both the rear wheel and the ground while pedaling was determined to be 29 inches (0.74 m).

A frame and rider harness were constructed, however preliminary rider satisfaction tests determined that the vehicle would require significant further development and extensive rider training before being competition-ready. Concurrent testing of the all-wheel steer concept discussed in section 2.5.2 proved it a more feasible design alternative. For these reasons, the team chose to delay further development of this design.

3.2.2 Foot Flaps Testing

Objective	Method	Results
Improve slow speed and zero speed stability by allowing rider's feet access to the ground.	Holes were designed into a previous vehicle with foot flaps to cover them when not in use. Emergency stopping scenarios were simulated.	Foot flaps were determined to provide adequate emergency stability, however more clearance around the front wheel was needed for ease-of-use. This was taken into consideration when designing the monocoque fairing.

The two dominant utility issues for the team have been ingress/egress and launching/stopping. Previous vehicles have only allowed access through the front hatch. Unless the rider is experienced, at least one person is needed outside the bike for adequate zero-speed stability. For this reason, the team tested the use of holes in the fairing to allow the rider to place their feet on the ground. To maintain aerodynamic efficiency, these holes would need to be covered when not in use.

Two concepts were tested: foot slits and foot flaps. Foot slits consisted of malleable fabric coverings, while foot flaps were rigid shells designed to pivot away from the rider's feet. Both concepts were tested using a frame mounted to the previous year's prototype. Riders were able to actuate both systems successfully. It was determined that the aerodynamics of the fairing could not be upheld by the foot slits, and so they were abandoned in favor of foot flaps.

A final design for foot flaps was tested with the 2012 Carnot Cycle. Holes were cut into the fairing and covered with prototype carbon fiber foot flaps, which were returned to position with a spring mount. The system was tested in simulated emergency stopping conditions and it was determined that the rib structure gave insufficient room for feet to pass the front wheel. Thus the gunwale rib structure would need to be moved outward from the bottom of the vehicle. Further simulated emergency stops proved that significant experience could mitigate this issue and that the foot flaps were a dependable alternative for low- and zero-speed stability, meeting the PDS of 1 falls in 10 starts and stops.

3.2.3 K.I.N.G.E.N. Testing

Objective	Method	Results
To determine the plausibility of using a control moment gyroscope system to stabilize a bicycle.	Build a prototype control momentum gyroscope system to stabilize a small upright bicycle.	The prototype control moment gyroscope system on a small bicycle that did not effectively stabilize it.

A control momentum gyroscope (CMG) consists of a flywheel and one or more motorized gimbals. These motorized gimbals can tilt the flywheel thereby causing a change in angular momentum. This change in angular momentum causes a gyroscopic torque that rotates the object attached to the CMG. A variation of a CMG has been used by Lit Motors to stabilize their C-1 motorcycle [14]. Other non-commercial CMG prototypes have also been developed for upright bikes.

To explore the possibility of using this technology for a recumbent bicycle, team members designed and build a prototype CMG for a miniature upright bike. This project was named the Kinetic Instrument to Navigate and Gyroscopically Enforce Normality (K.I.N.G.E.N.). The K.I.N.G.E.N.'s

flywheel was attached to a fork, which was attached to a stepper motor. This stepper motor was fixed to the bike frame. An accelerometer was also fixed to the bike frame. A basic schematic of the K.I.N.G.E.N. and a detailed schematic of the flywheel are shown in Appendix C. A picture of the prototype system is shown in Figure 18 below.



Figure 18. Prototype KINGEN Stability System.

This accelerometer measured the angle of the bike to the ground (upright was 0°). A microcontroller took input from the accelerometer and directed the stepper motor to turn. The turning of the stepper motor turned the flywheel, which caused a gyroscopic torque on the bike that was designed to right it. A PI microcontroller was implemented to make this possible.

Unfortunately, K.I.N.G.E.N. was unsuccessful for a few reasons. First, the microcontroller did not react quickly enough. The mass of the flywheel was also too great, which caused too strong of a torque to be imparted on the bike, even with the smallest of the stepper motor’s rotations. Finally, the PI controller was not robust enough to be effective. The K.I.N.G.E.N has future potential if these problems are addressed.

3.2.4 Rib Modification Testing

Objective	Method	Results
Test the effectiveness of chopped-strand carbon fiber rib repair	4-point bending test rib samples to failure, repair the ribs, perform a second bending test to failure	A significant portion of the ribs strength was returned and statistical analysis yielded no meaningful difference between the two values. Further testing is recommended.
Determine if rib stapling method weakens structural elements.	Stapled ribs were tested to failure in a 4-point bending test, repaired, and then tested a second time. Mean bending strength was compared to the control data.	The ribs likely retained most of their strength based on observed failure modes; statistical analysis yielded no meaningful difference between stapled and control ribs. Further testing is recommended.

For this testing, several 1 in (25.4 mm) rib samples were created by wrapping Nomex in unidirectional carbon fiber between sheets of woven carbon fiber. These ribs are the control ribs and are the baseline for further testing. The first modification tested was repair of failed ribs. The control ribs were tested in

bending with a four-point bending tester. After the ribs failed, the failure point was cleared and filled with chopped-strand carbon fiber saturated with epoxy. A sample of a repaired rib is shown in Figure 19. The patched ribs were crush tested again after the repair cured fully. This test was conducted with the center of the four-point bending tester spanning the repaired section. For ribs 1 and 2, the ribs failed at a location other than at the patched location, suggesting that the repair may be satisfactory in compressive bending. Data for this test is included in Table 10

The second rib modification tested was a rib that had been stapled in place on a mold surface. This test was performed to determine if staples could be used to hold structural elements to the mold during the layup process. The stapled ribs were created on an old mold surface and tested in the four-point bending tester after they fully cured. This test was conducted with the center of the four-point bending tester spanning a stapled section of the rib. A sample rib with a stapled section highlighted is shown in Figure 20. None of the specimens failed at the staple region, suggesting that the staple method does not cause stress concentrations. Data for this test is included in Table 10.

Table 10. Failure Point of Ribs, Repaired Ribs, and Stapled Ribs

Rib	Rib Failure Point (lbs)	Repaired Rib Failure Point (lbs)	Stapled Rib Failure Point (lbs)
1	149	138	154
2	179	149	141
3	149	98	116



Figure 19. Sample Rib with Epoxy, Chopped Fiber Repair.

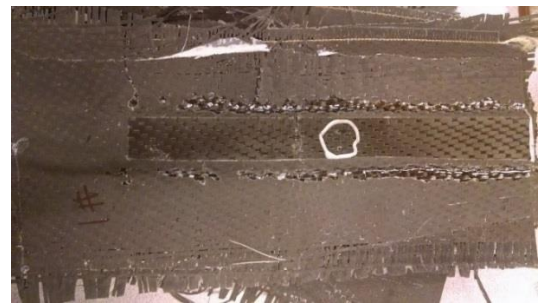


Figure 20. Sample Rib with Staple, circled in white

Assuming an underlying normal distribution of failure forces, we used paired Student's t-tests to test the following two hypotheses: (a) that there is a difference in the mean ultimate strength for the original ribs and the repaired ribs, and (b) there is a difference between the mean ultimate strength of the original ribs and the stapled ribs. For the repaired ribs the team obtained a p-value of 0.117, and for the stapled ribs we obtained a p-value of 0.247. In both cases, we therefore failed to reject the null hypothesis at the 5% level that there is a difference between the mean failure forces for the repaired or stapled ribs. While the absolute differences in the failure forces are considerable, the small sample size of $n=3$ creates large uncertainty. In future years, the team plans to perform more of these failure tests which would be likelier to provide a more conclusive answer.

Table 11. Two-sample T for Failure Point (lbs) vs Stapled Rib Failure Point

Failure Point (lbs)	N	Mean (lbs)	Standard Deviation	SEM
Regular Rib Failure Point	3	159.0	17.3	10
Stapled Rib Repair Failure Point	3	137.0	19.3	11

3.2.5 Pneumatic Landing Gear Testing

Objective	Method	Results
Test the suitability of a pneumatic landing gear system for the HPVC	Design and construct a prototype landing gear system. Actuate the landing gear to determine speed, air requirements, and durability.	The pneumatic landing gear proved suitable for the HPVC regarding air requirements and speed of actuation, but design modifications must be made to ensure durability.

The team tested the pneumatic landing gear system for feasibility, durability, speed of actuation, and reliability. The pneumatic actuator was attached to the telescoping tubing of a previous year's landing gear in place of an electronic actuating method. This allowed for testing of the speed at which the landing gear actuated and the number of actuations per tank of air. The previous electronically controlled landing gear could actuate in approximately 2 seconds. In contrast, the pneumatic system actuated in 0.16 seconds, as determined from high-speed video of an actuation sequence. The landing gear is estimated to actuate 100 times in a given endurance race, and so the team required the prototype to actuate 100 times on one tank of air. The piston was connected to a tank initially at 3000 psi. After 100 tests, the tank was at approximately 2200 psi, which is above the minimum required pressure of 150 psi for the pneumatic piston, meaning that air remained in the system.

From this testing, the team concluded that the pneumatic landing gear concept was a feasible design, and was more practical than other options due to its rapid and predictable actuation. The team identified several design challenges regarding the system, most notably that the piston actuated too rapidly and tended to damage the apparatus when fully extending. The team plans to mitigate this with flow restrictors attached to the actuating solenoid.

3.2.6 Motion Capture

Objective	Method	Results
Determine the volume required by a rider pedaling in the recumbent position for use in aerodynamic analysis.	Capture the motion of riders at anthropomorphic extremes riding in the recumbent position on a trainer adjusted to the geometry of the vehicle.	A solid model of the rider while pedaling was determined.

To ensure reasonable clearances between the rider and the fairing, data was collected from three test subjects riding a customizable recumbent trainer. The test subjects represented the anthropomorphic extremes of this year's potential riders. Three Qualisys Track Manager IR cameras recorded the spatial coordinates of reflective balls placed on each rider's joints, as shown in Figure 21. Although similar tests were performed in the design of the 2012 Carnot Cycle, increased accuracy was achieved by repeating motion capture with the new seat position. Because pedaling motion differed with speed, each rider was recorded as they started to pedal, maintained a comfortable long-distance pace, and then sprinted. A MATLAB program used these points to determine the volume riders used while pedaling and represented this data as a wireframe model. The shape of the fairing was designed around this frame, shown in Figure 22. This solid model will allow for a fairing which fits the rider well, meeting the PDS of rider satisfaction.

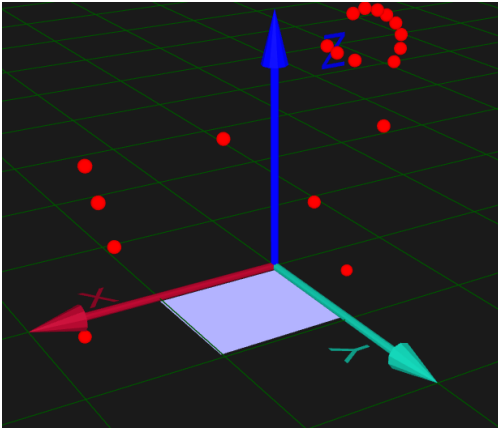


Figure 21. Spatial Coordinates of Dots

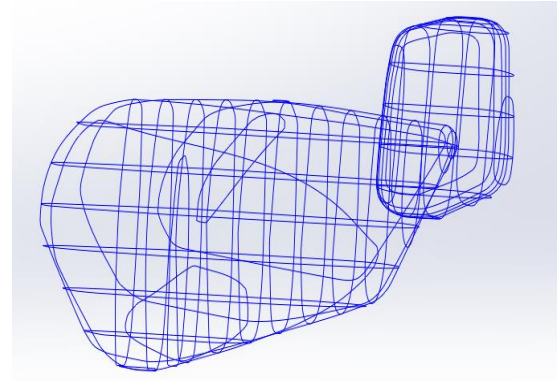


Figure 22. Wireframe of Vehicle

3.2.7 Layup Testing

Objective	Method	Results
Improve lamination of the vehicle's composite structure.	Iterative development of a bagging system capable of creating the required vacuum for lamination and conforming to all surfaces.	A dual-bagging method was developed which resulted in greatly increased vacuum pressures. Stretchlon was determined to be an appropriately conformable bagging film for use in team layups.

For Shannon-igans, the team iterated several improvements to the layup process. The preliminary test was to determine if the layup box previously used could be sealed to provide adequate vacuum. Four-inch squares of plywood were sealed using a collection of sealants including epoxy resin, shellac, and polyurethane. It was determined that epoxy resin produced an adequate vacuum seal with less than 1 inch of mercury drop from full vacuum. This sealing method was then tested on a full-scale box, but proved to be inadequate, with a total drop of 20 inches of mercury from full vacuum. Upon failure of this test, a dual-bag method was developed to seal the molds. Similar to the 2014 Namazu, both the interior and exterior of the mold was sealed. To improve the vacuum on the interior surface the exterior surface was sealed with a separate bag and evacuated using a separate vacuum pump. This method proved adequate with a total drop of 1 inch of mercury from full vacuum on the interior surface.

Finally, the team tested the use of Stretchlon 200 bagging film during the layup process to decrease the precision required when constructing bags. The published specifications for Stretchlon 200 bagging film state a 500% increase in length, however research suggested that the actual performance of this was much lower [15]. To test the expansion by area, the film was applied to the opening of a 19-inch plastic drum, the air was evacuated, and depth of stretch before rupture was determined. Over a series of 3 trials, the average depth of stretch was 19.5 in (49.5 cm). Assuming a normal hyperbolic shape under tension, this represents an increase in surface area of 250%. Although significantly lower than the published specifications, the team determined that this performance was adequate, and used the film during the layup process, obtaining better composite lamination. This testing resulted in production of lighter weight composites, meeting the PDS of vehicle weight.

3.3 Performance Testing

3.3.1 HPVC Obstacle Testing

Objective	Method	Results
Test the vehicle readiness for competition obstacles.	Ride the prototype through simulated obstacles and compare to performance of previous vehicles.	The vehicle is not slower than previous vehicles, and the AWS system is significantly faster through the hairpin turn.

The team tested the prototype against different obstacles to determine Shannon-igans' readiness for the 2015 HPVC. The team timed the riders on the Shannon-igans prototype racing through the slalom and hairpin turns with and without AWS. The results of this testing are included in Table 12. Assuming an underlying normal distribution of trial times, we used paired Student's t-tests to ascertain if there is significant difference in speeds of Shannon-igans through each obstacle with and without AWS. For the AWS active in the hairpin turn, we rejected the null hypothesis at the 5% level, meaning that the vehicle is faster with AWS through this obstacle. For all other tests, we failed to reject the null hypothesis. The small sample size of $n=3$ creates large uncertainty for most measurements. In future years, the team plans to obtain a larger pool of data, which would provide a very conclusive answer.

Table 12. Average Slalom and Hairpin Times with Standard Deviations

Bike	Slalom (Average time seconds)	Hairpin (Average time seconds)
Ragnarök Prototype (2010)	8.3 +/- 0.6	3.12 +/- 0.08
Ragnarök (2010)	8.1 +/- 0.4	2.6 +/- 0.3
Shannon-igans Prototype without AWS	7.6 +/- 0.4	2.2 +/- 0.1
Shannon-igans Prototype with AWS	8.2 +/- 0.1	1.1 +/- 0.1

3.3.2 Rear Wheel Turning Radius Testing

Objective	Method	Results
Test the turning radius benefit of the AWS system.	Attempt the tightest possible turn at 10 mph. Compare to previous vehicles.	AWS was determined to increase maneuverability by 60%, making the vehicle perform favorably to previous years.

The team tested the turning radius of the Shannon-igans prototype to approximate the turning radius of the final vehicle so that it would meet the turning radius PDS. During testing the team found that with the AWS inactive the turning radius was 9 ft (2.74 m) and with the AWS active the turning radius was 3.58 ft (1.09 m) giving the vehicle a 39% increase in turning radius with the system active. Additionally the team compared the Shannon-igans Prototype to the team's previous vehicles showing that the Shannon-igans Prototype turns tighter than all but the upright bicycle.

Table 13. Turning Radius of Previous Vehicles

Vehicle	Smallest Comfortable Turning Radius (in)
2013 Celeritas	156
Shannon-igans Prototype, AWS inactive	108
2014 Namazu Prototype, rear wheel steering	45
Shannon-igans Prototype, AWS active	42
Upright bicycle	35

3.3.3 All-Wheel Steer Durability Testing

Objective	Method	Results
Determine likely failure modes of the AWS system.	Test the system for 100 miles of riding (160 km) and note any failures	Failures were noted and fixes were identified

The team conducted significant durability testing on the AWS system to ensure it would operate throughout the competition and daily use. The prototype vehicle was ridden more than 100 miles over a period of several months, allowing time for durability problems to surface. Several problems were identified, summarized in Table 14 below alongside each solution implemented.

Table 14. Safety Features of an All Wheel Steer System

Component:	Failure mode(s):	Solution(s):
Joystick wiring	Break in wiring harness	Electronics and software implemented to detect problem and shut down AWS system with wheel centered until fixed
Servo	Servo breaks or is otherwise compromised	Rear fork designed with zero trail to prevent unpowered steering.
Battery	Low battery voltage	System tracks battery voltage; automatically centers wheel and shuts down before voltage drops too low
Human Interface	Accidental bump of joystick	Software filtering mitigates small bumps, speed sensitivity reduces detrimental action at high speeds, system automatically shuts off above 30 mph
Control Circuitry	Malfunction of the control circuitry	A manual on-off switch mounted to the tiller allows the rider to cut all power to the AWS system in the event of a control circuitry malfunction

3.3.4 Coastdown Testing

Objective	Method	Results
Determine the appropriate tire pressure for use in the HPVC to decrease rolling resistance.	Coastdown testing was performed at different tire pressures and analysis was performed to extract the rolling resistance	The data obtained were too noisy to yield useful results. The team recommends further testing in a controlled environment.

To determine the most efficient tire pressure for the tires of the Shannon-igans, the team conducted coastdown testing. This experiment was designed based on SAE coastdown standards. The 2012 Carnot Cycle was used with a set of Durano tires inflated to 5.2 bar (75 psi), 6.6 bar (95 psi), and 7.9 bar (115 psi). The experiment was done on a level section of a local asphalt bicycle trail. A series of 12 trials were run at each tire pressure, alternating directions with each run. The coefficient of rolling-resistance was calculated for each tire pressure. Sophisticated statistical analysis was used to determine the uncertainty in the resultants, since the analysis method involved curve fitting a 2nd order Data Reduction Equation to the velocity data (see Appendix D of Appendix D). The team concluded that this experiment could not differentiate between tire pressures due to a large uncertainty, which was specifically due to neglecting the effect of course slope and minor differences in pavement. The team's recommendation is that future experiments in this area use a dedicated testing machine, allowing for more control over the testing conditions and giving results that can be compared across different tires.

4 Safety

4.1 Design Safety

4.1.1 Roll Bar

To protect the rider in the event of a side impact or overturning, the Shannon-igans contains a composite roll bar. The roll bar decreases the severity of a crash and keeps the rider from impacting the surface of the road. The composition of the roll bar is depicted in Section 1.7.2.

4.1.2 Steering System

The All-Wheel Steer system poses a unique safety challenge for Shannon-igans, as a problem with the system while riding could cause the rider to lose control and possibly crash. With this in mind, every component of the system has been evaluated, failure modes determined, and safety solutions enacted. Many of the potential problems were discovered and ameliorated during the testing of the prototype, as shown in Section 3.3.3.

Standard electrical safety precautions have also been taken. The highest voltage in the system is 12 volts, reducing the chance of electrical shock. All electrical systems and subsystems are properly fused to protect the electronics and the rider in case of an electrical short circuit. All wiring is encased in abrasion resistant looms, well secured, and routed in protected areas to prevent damage. In the event of a catastrophic failure of the system, a pin can be inserted into the rear fork, locking it in place and causing Shannon-igans to perform as a normal recumbent.

4.1.3 Seat Belt

The seat belt on Shannon-igans is a three-point harness similar to that used on the 2014 Namazu. It was chosen due to low cost and fast ingress and egress. It is secured in the same fashion as the 2014 Namazu, with all three attachment points riveted between the roll bar and a steel cap plate. This attachment method was tested to ASME HPVC specifications for the 2012 Carnot Cycle [4].

4.1.4 Windshield

The vehicle's windshield is made out of polycarbonate to ensure its durability and protection of the rider. The windshield enables 200 degrees of visibility, allowing the rider to see more than just what is straight ahead. With the rearview mirrors, the rider has a field of vision of 300 degrees. The vehicle's field of vision meets the 180 degree requirement for the ASME HPVC [6].

4.1.5 Safety of Manufacturing

The team takes safety very seriously and makes sure that all members are educated on the proper use of power tools and machines. Members are required to have supervision when using machines and to use proper personal protective equipment (PPE). Examples of PPE include respirators when sanding or dremeling composites, welding equipment when MIG welding, and safety glasses.

4.2 Hazard Analysis

Rider safety during races is the team's number one priority. All riders are required to wear a helmet when using any of the team vehicles. Flanges extend forward from the roll bar protect riders' arms during a crash with the top fairing removed. Kevlar 5120 fabric lines the cockpit where the rider sits. In the event that the carbon fiber splinters, the Kevlar traps the splinters and prevents rider injury [2]. Sharp edges developed during the manufacturing process are removed or covered by rounded edging. Uncontrolled skidding after a fall can be more dangerous than the fall itself with the rider unable to control the path that the vehicle takes. To reduce skidding, neoprene rubber was attached to the fairing at the points which contact the ground in a crash.

To help the rider communicate their intentions and make their presence known to other vehicles and pedestrians, standard equipment such as headlights, taillights, brake lights, turn signals, side reflectors, and a loud horn have been installed. The vehicle's low height makes it less visible on the road, and therefore to improve the visibility of the vehicle, a safety flag mount is installed in the rear of the vehicle, and a 5-foot safety flag is available for use while riding.

5 Conclusion

5.1 Comparison

Table 15. Evaluation of Shannon-igans against PDS

Metric	Marginal/Target Value	Actual Value	In-Text Justification
Falls in 20 stops and starts	1/0	0	Slalom Testing
C_dA (ft ²)	1.2/0.60	0.085	Aerodynamic Analysis
Part count	100/80	85	
Drivetrain efficiency	90/98	93	Drivetrain
Rider satisfaction (1-10 scale)	7/10	8	
Field of view (deg)	180/360	200	Windshield
Time to enter/exit (s)	15/3	10	Fairing and Frame Design
Turning radius (ft)	15/6	3.7	Turning Radius Testing
Weight (lbf)	80/50	70	
Construction time (weeks)	7/5	7	Organizational Timeline
Cost (excluding labor)	\$7,000/\$5,000	\$4,901	Cost Analysis

5.2 Evaluation

Shannon-igans was not completed by the submission of this report, but it has met or is expected to meet all applicable PDS. Furthermore, Shannon-igans either currently meets or will meet all constraints imposed by HPVC, Rose-Hulman, HPRA and Indiana state law.

5.3 Recommendations

The team recommends performing stability analysis concurrently with fairing design to optimize both aerodynamics and stability. If not previously constrained, stability analysis would have recommended a longer distance from the rider center of gravity to the front wheel and shorter distance from the rider center of gravity to the rear wheel. The team also recommends performing wind tunnel testing on a scaled model of its vehicles prior to the onset of manufacturing to verify CFD models before it is too late to change. The team was unable to perform this testing this year because of time constraints. It would also be very beneficial for Shannon-igans to be put through a coastdown test after the 2014/2015 HPVC and for the uncertainty in this test to be decreased. Nose cone testing did not produce any design modifications to Shannon-igans, but the team recommends that work continues on the concept.

5.4 Conclusion

The Rose-Hulman Human Powered Vehicle Team set out to create an efficient, fast, and practical human powered vehicle that could be safely and effectively used for everyday transportation. Meeting these goals required a lightweight vehicle, so Shannon-igans uses advanced composite materials for an exceptional strength-to-weight ratio in its fully structural fairing. Shannon-igans is highly efficient compared to an upright bicycle, requiring seven times less power to overcome air drag at regular travel speeds of 20 mph (32 kph). It can travel over 45 mph (74 kph) due to its streamlined body, yet it has excellent maneuverability with its all-wheel steering mechanism. By employing several methods,

Shannon-igans is very stable at zero-speed in comparison to previous vehicles produced by the team. Most importantly, it protects the rider with its rollover protection system, safety harness, and Kevlar lining. Shannon-igans' combination of efficiency, safety, and practicality makes it a viable form of everyday transportation.

References

- [1] National Highway Traffic Safety Administration, "SAFETY 1N NUM3ERS," 2014. Available: www.nhtsa.gov/nhtsa/Safety1nNum3ers/july2014/S1N_Bicycles_812047.pdf
- [2] Rose-Hulman Human Powered Vehicle Team, "2010 HPVT Design Report- West - Ragnarök," Terre Haute, 2010.
- [3] Rose-Hulman Human Powered Vehicle Team, "2011 HPVT Design Report - West - Helios," Terre Haute, 2011.
- [4] Rose-Hulman Human Powered Vehicle Team, "2012 HPVT Design Report - West - Carnot Cycle," Terre Haute, 2012.
- [5] Rose-Hulman Human Powered Vehicle Team, "2013 HPVT Design Report - West - Celeritas," Terre Haute, 2013.
- [6] American Society of Mechanical Engineers, "Rules for the 2015 Human Powered Vehicle Challenge," 2015.
- [7] Indiana State Legislature, "Chapter 11: Bicycles and Motorized Bicycles," 2013. [Online]. Available: <http://www.in.gov/legislative/ic/2010/title9/ar21/ch11.html>.
- [8] Human Powered Race America, "Classes and Rules," 2015. [Online]. Available: <http://www.recumbents.com/hpra/hprarules.htm>
- [9] Rose-Hulman Human Powered Vehicle Team, "2014 HPVT Design Report- West -Namazu," Terre Haute, 2014.
- [10] Cycling Power Lab, "Drivetrain Efficiency & Marginal Gains", 2014. [Online]. Available: <http://www.cyclingpowerlab.com/drivetrainefficiency.aspx>.

[11] J.M Corum, R.L Battiste, K.C. Liu, M.B. Ruggles, “Basic Properties of Reference Crossply Carbon-Fiber Composite”, Feb 2000. [Online].

Available: web.ornl.gov/~webworks/cpr/v823/rpt/106099.pdf

[12] Performance Composites, “Mechanical Properties of Carbon Fibre Composite Materials, Fibre / Epoxy resin”, July 2009. [Online].

Available: http://www.performance-composites.com/carbonfibre/mechanicalproperties_2.asp

[13] S. Friedlander, "Lightning Bikes," [Online]. Available:

<http://www.lightningbikes.com/f40/friedlander-testimonial.html>.

[14] C1: Lit Motors: Gyroscopic Stability [Online]. Available: <http://litmotors.com/c1/>

[15] Fibre Glast: Stretchlon® 200 Bagging Film [Online]. Available:

http://www.fibreglast.com/product/stretchlon-200-bagging-film-1678/Vacuum_Bagging_Films_Peel_Ply_Tapes

Appendix A: Enumerated Cost Analysis

Item	Cost	Amount Per Vehicle (If Consumable)	Price Per Vehicle	Price for Production Run
5 CFM Air Compressor	\$550.00	-	-	\$1,650.00
Bicycle Mechanic Toolset	\$350.00	-	-	\$1,050.00
3.2 CFM Venturi Pump	\$180.00	-	-	\$540.00
HSS Drill Index	\$115.00	-	-	\$345.00
18v Cordless Drill	\$105.00	-	-	\$315.00
Welding Jacket (5 ct)	\$88.75	-	-	\$266.25
Welding Gloves (6 ct)	\$84.00	-	-	\$252.00
50 ft Air Hose	\$66.00	-	-	\$198.00
End Mill Set	\$59.80	-	-	\$179.40
Carbide Tool Inserts (10 Ct)	\$45.00	0.5	\$22.50	\$4,050.00
Safety Glasses (50 ct)	\$41.50	-	-	\$124.50
Dremel Rotary Tool	\$41.00	-	-	\$123.00
6 Inch Air Powered Rotary Sander	\$40.00	-	-	\$120.00
Tap and Die Set	\$39.99	-	-	\$119.97
Carbide Lathe Tools	\$37.00	-	-	\$111.00
Latex Gloves (100 ct)	\$35.00	0.25	\$8.75	\$1,575.00
Duct Tape 2 in x 25 yd (6 ct)	\$30.00	0.5	\$15.00	\$2,700.00
Dremel 1-1/2 Inch Cutting Wheel (12 Ct)	\$20.00	1	\$20.00	\$3,600.00
120 Grit Sanding Discs (25 Ct)	\$16.00	1	\$16.00	\$2,880.00
Rivet Gun	\$10.00	0.25	\$2.50	\$450.00
Popsicle Sticks (500 ct)	\$8.50	0.1	\$0.85	\$153.00
1/8" Rivets (250 ct)	\$7.90	0.2	\$1.58	\$284.40
Silver Sharpies (6 Ct)	\$7.23	1	\$7.23	\$1,301.40
Plastic Cups (50 ct)	\$6.50	0.5	\$3.25	\$585.00
			Total Cost	\$22,972.92

Table A2: Capital Investments Required for Namazu Production Run

Item	Cost
5000 SF Industrial Space (3-year lease)	\$27,500
12-Inch Shop Lathe	\$2,800
12-Inch 3-Axis CNC Mill	\$5,000
Floorstanding Drill Press	\$1,200
60 x 30 Wood Workbench (6 total)	\$1,400
Desktop Computer for CNC/CAD	\$800
Millermatic 350 MIG Welder	\$4,000

4 ft x 2.5 ft Welding and Jigging Table	\$2,400
JET 42-Inch Milling Machine	\$8,900
Total Capital Investment	\$54,000

Table A3: Overhead Costs for Namazu Production Run

Staff Overhead		
	Secretary	1
	Sales Staff	1
	Wage	\$25.00
	Manager	1
	Salary	\$80,000.00
	Staff Overhead Sub Total:	\$380,000.00
Salary Overhead		
	Total Wages	\$1,424,000.00
	State/Federal Tax Rate	15%
	Taxes	\$213,600.00
	Salary Overhead Sub Total:	\$213,600.00
Office Facilities		
	Office Rate (\$/SF/yr)	\$11.00
	Office Space (SF)	1000
	Office Cost	\$11,000.00
	Facilities Sub Total:	\$11,000.00
Utilities		
	Monthly power rate	\$100.00
	Monthly water rate	\$50.00
	Phone and internet rate	\$100.00
	Utilities Sub Total:	\$9,000.00
Insurance		
	Estimate	\$25,000.00
	Insurance Sub Total:	\$25,000.00
	Overhead Sub Total:	\$638,600.00

Appendix B: Rear Fork Structural Analysis Bulk Results

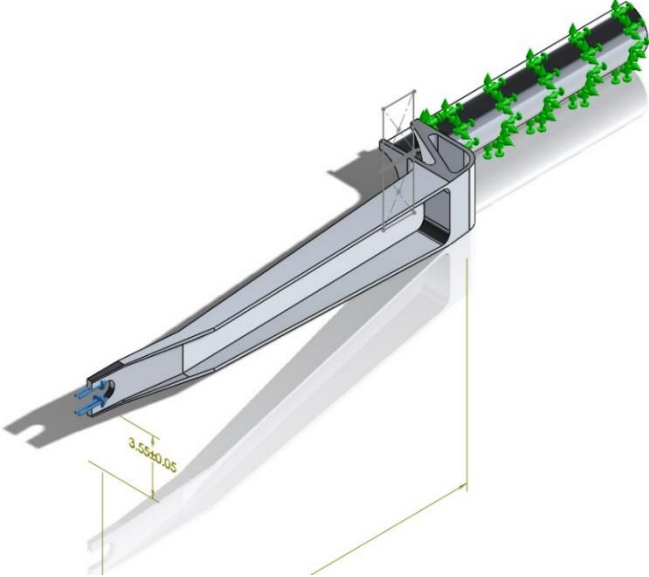


Figure 19. SolidWorks Axial Load Case Overview

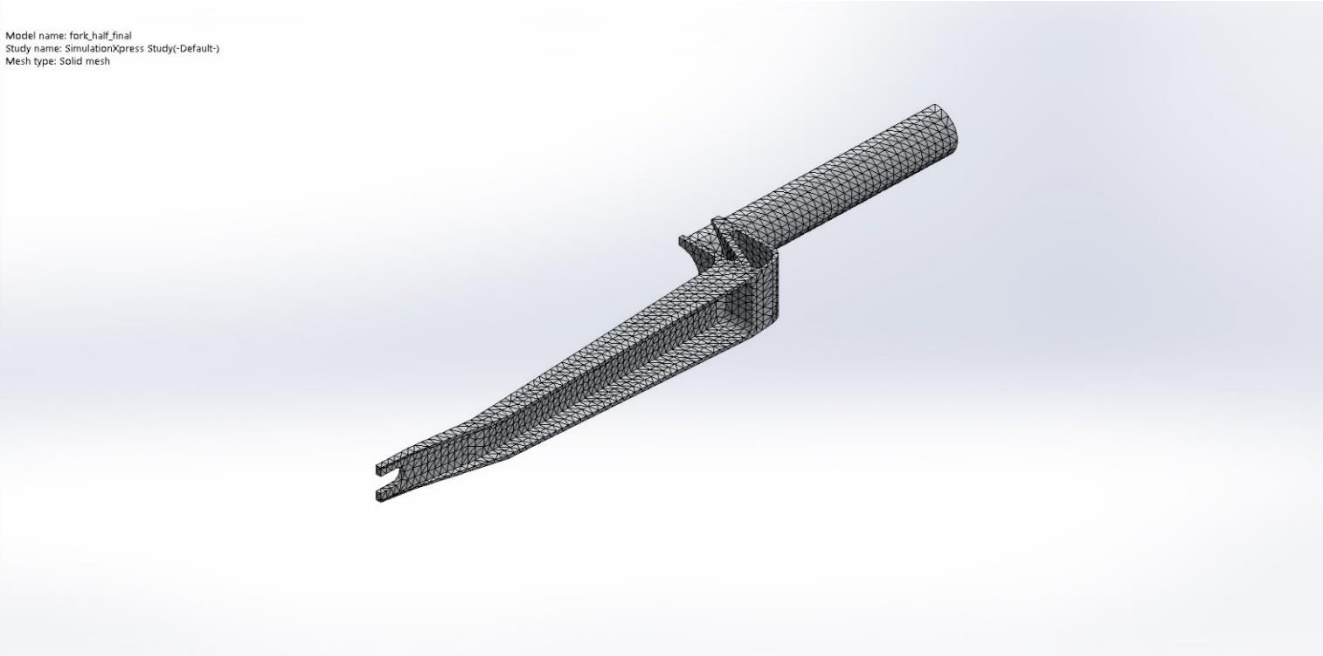


Figure 20. SolidWorks Axial Load Case Mesh

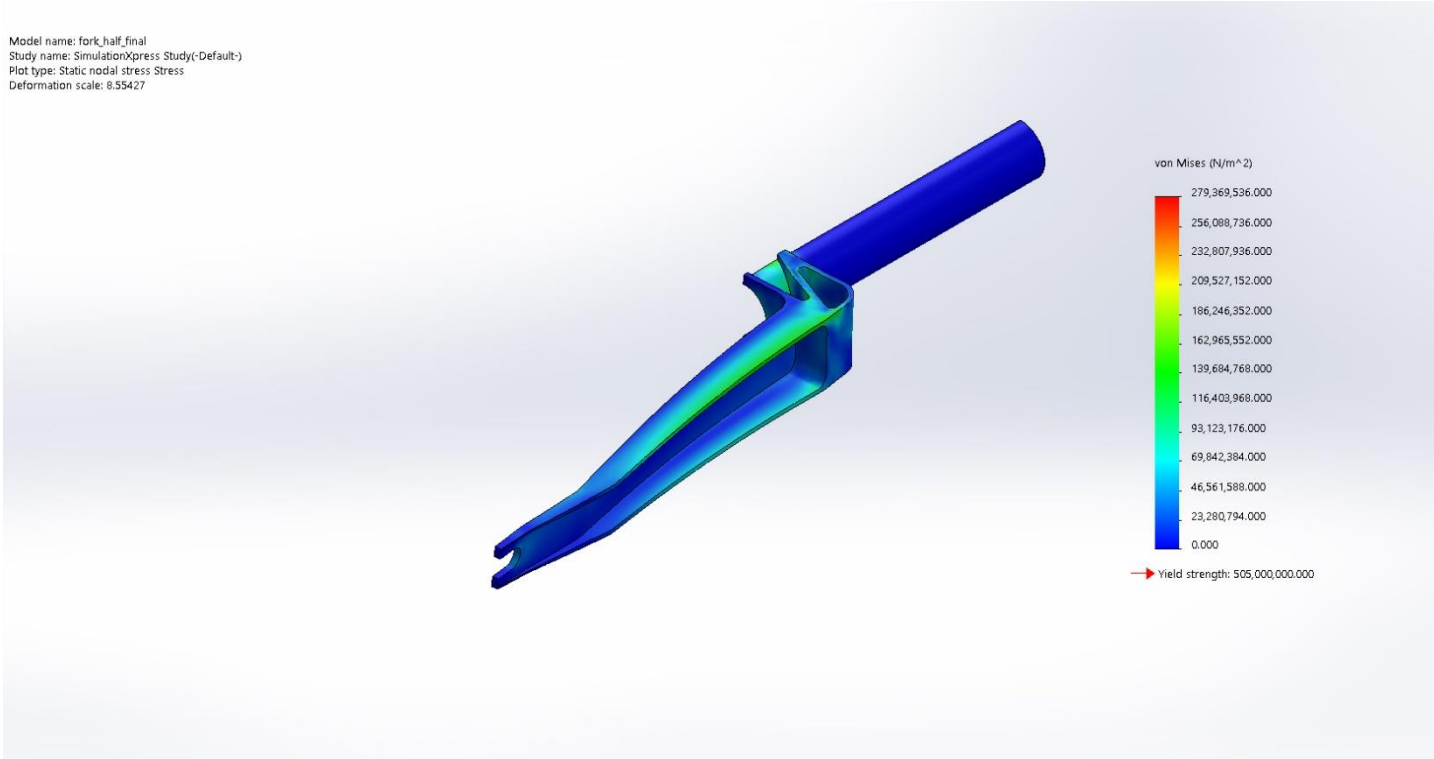


Figure 21. SolidWorks Axial Load Case von Mises Stress

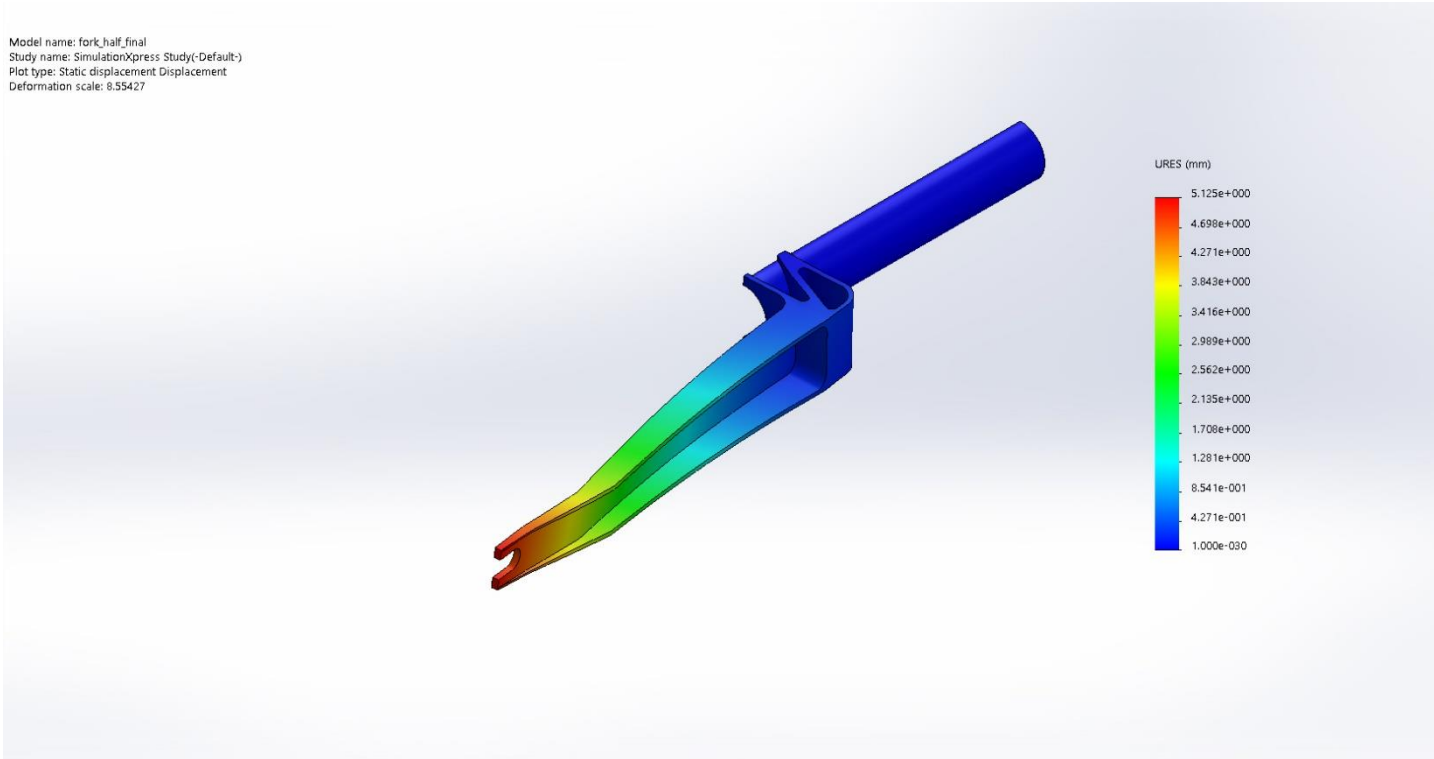


Figure 22. SolidWorks Axial Load Case Total Deformation

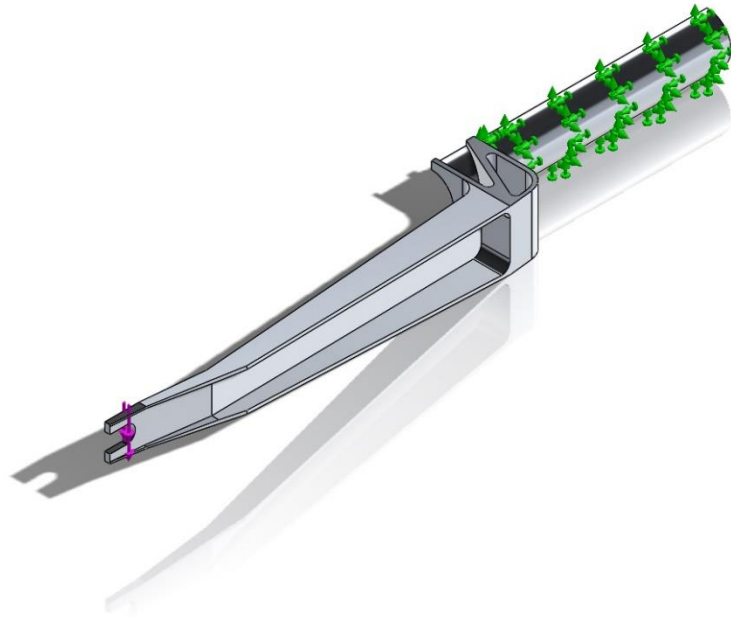


Figure 23. SolidWorks Bending Load Case Overview

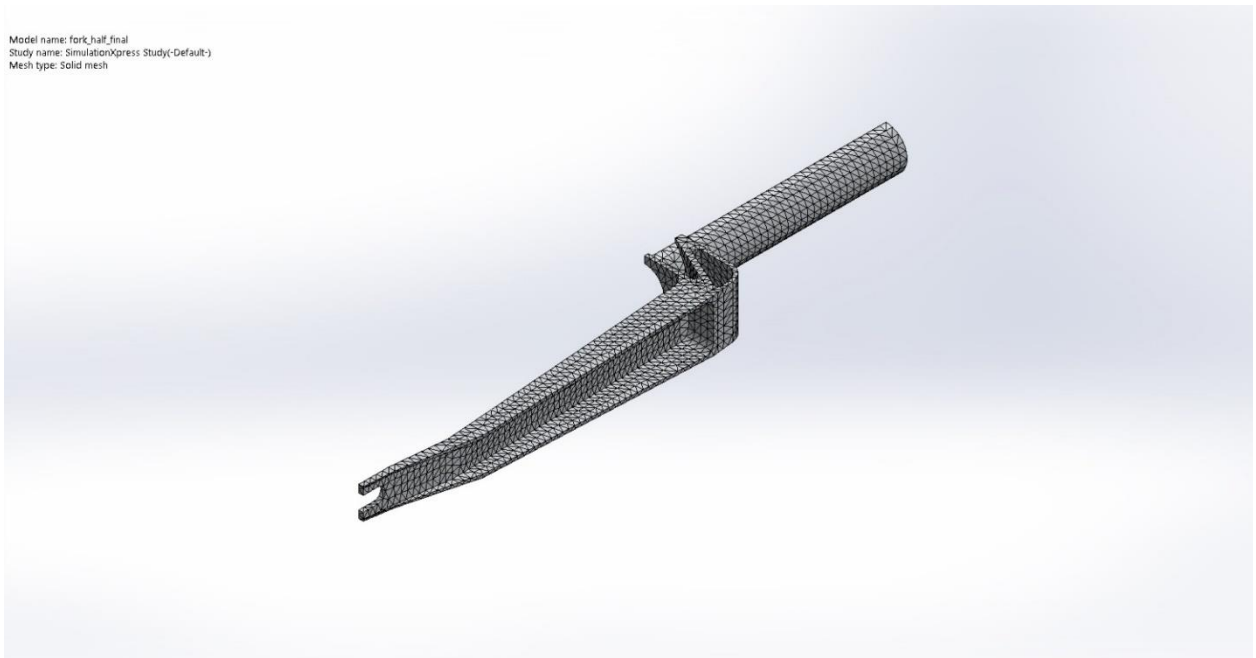


Figure 24. SolidWorks Bending Load Case Mesh

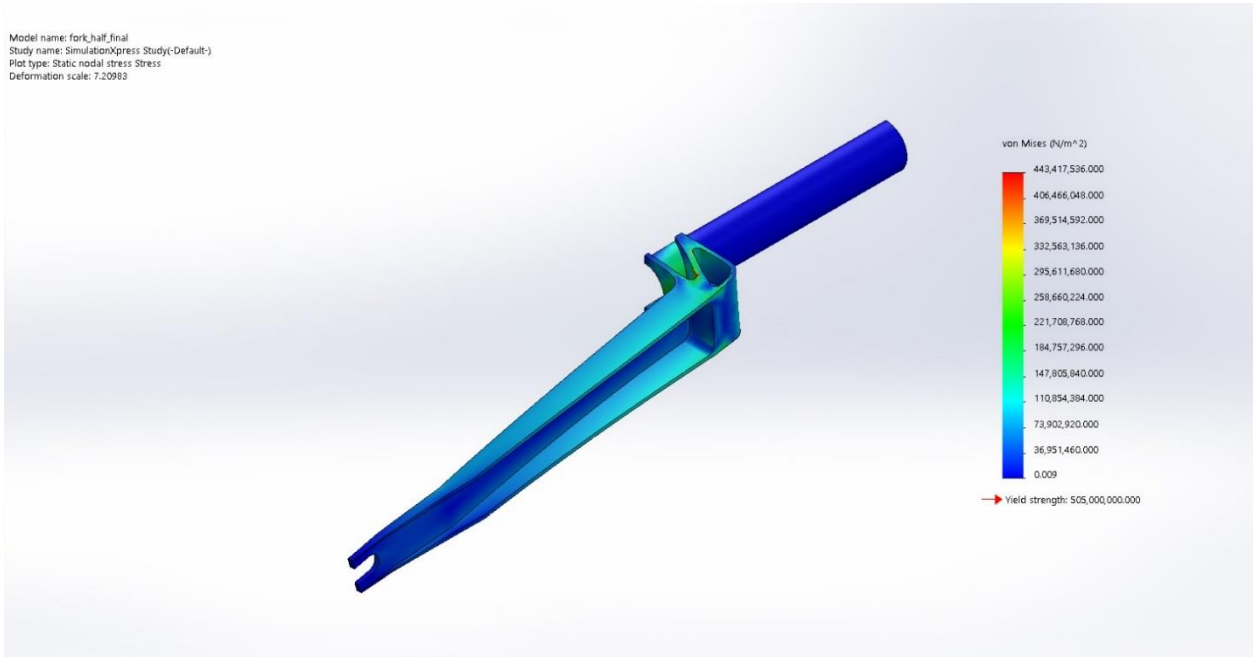


Figure 25. SolidWorks Bending Load Case von Mises Stress

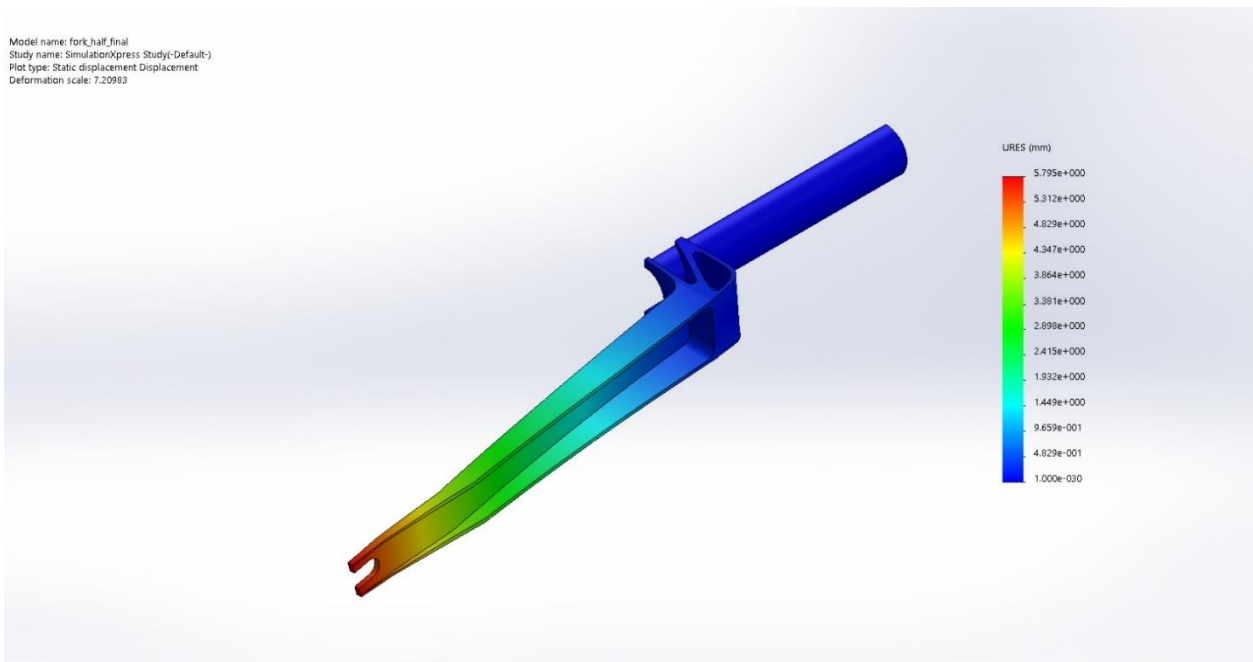


Figure 26. SolidWorks Bending Load Case Total Deformation

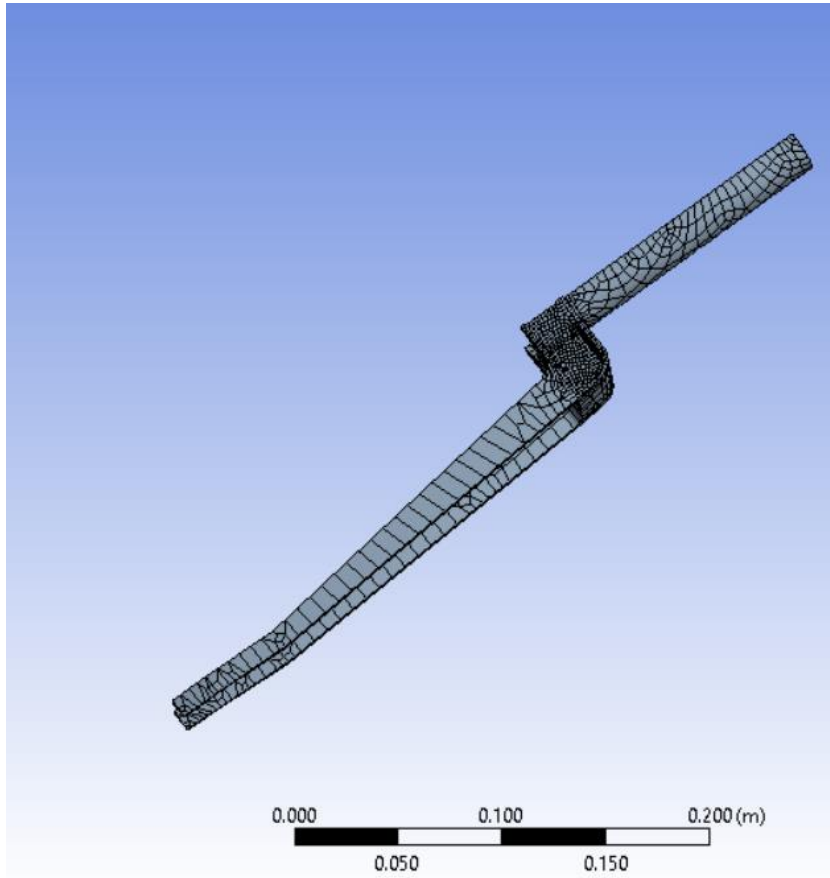


Figure 27. ANSYS Mechanical Mesh

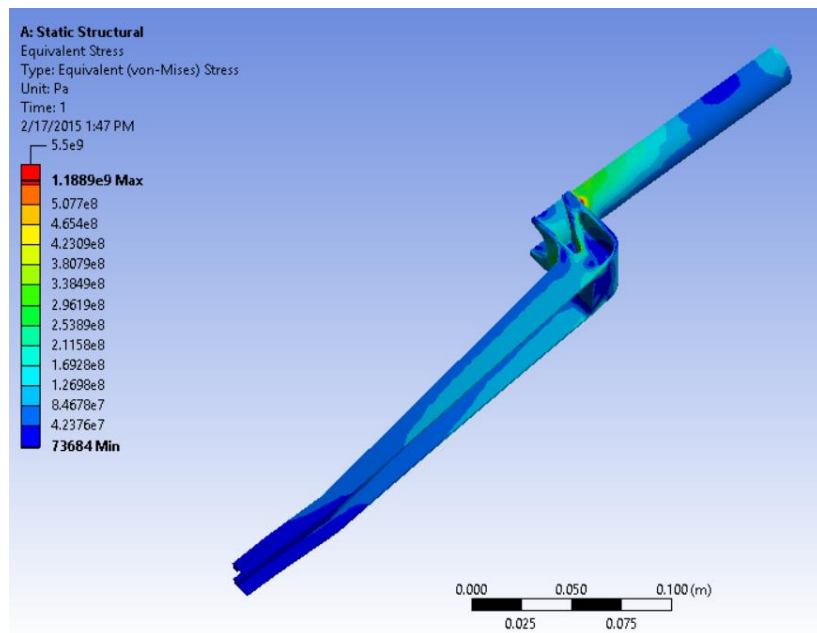


Figure 28. ANSYS Mechanical Bending Load Case von Mises Stress

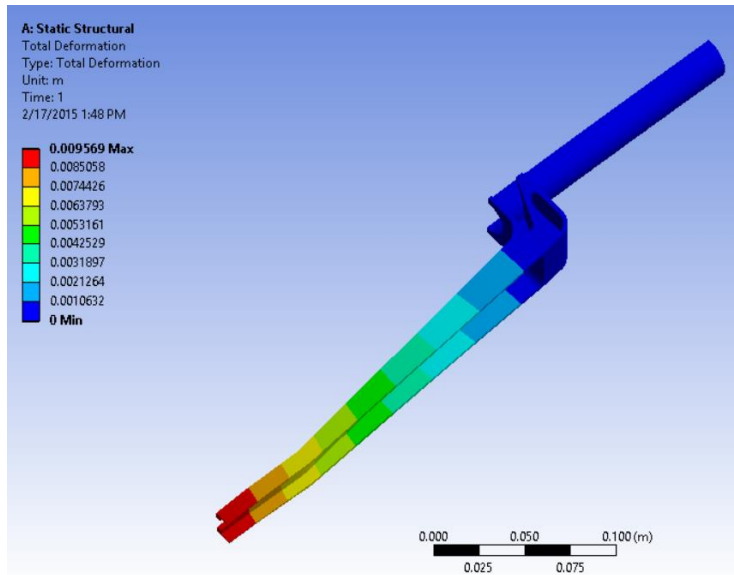


Figure 29. ANSYS Mechanical Bending Load Case Total Deformation

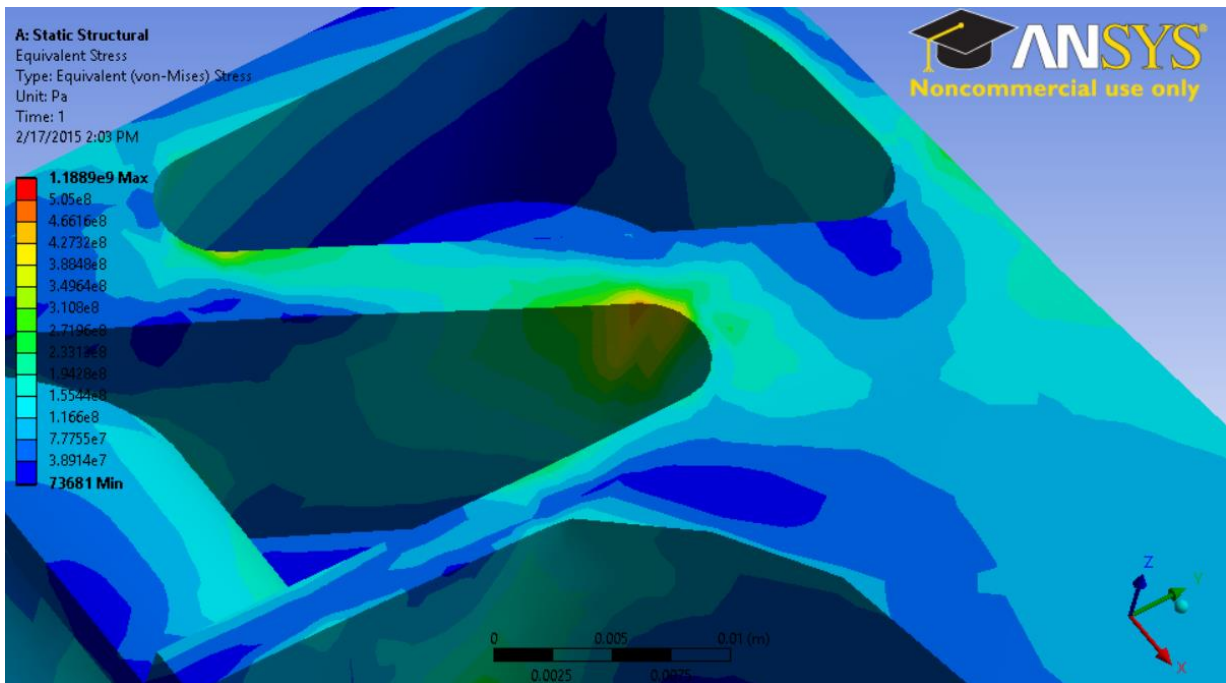


Figure 30. ANSYS Mechanical Bending Load Case Observed Stress Concentration

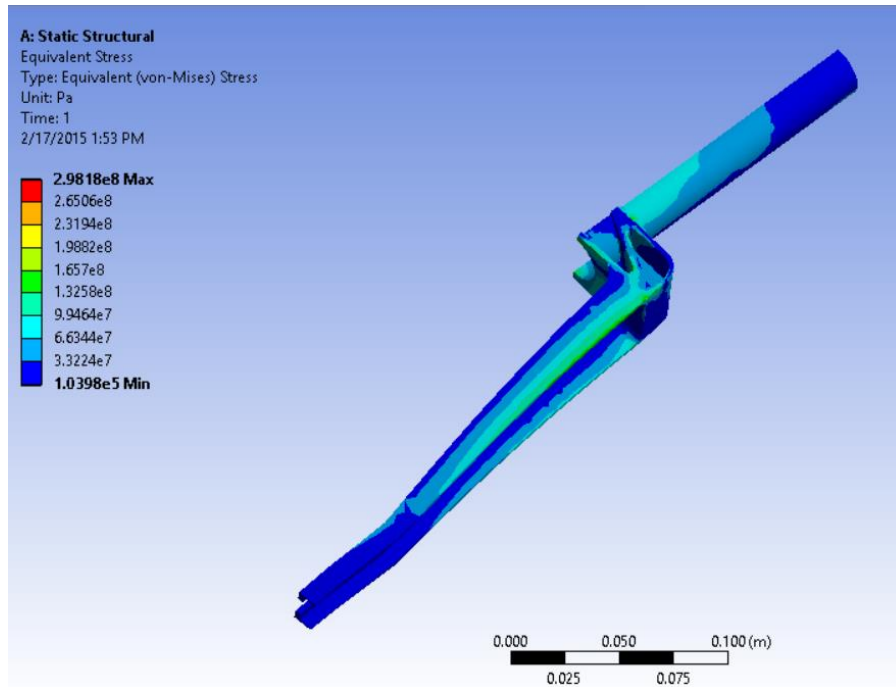


Figure 31. ANSYS Mechanical Axial Load Case von Mises Stress

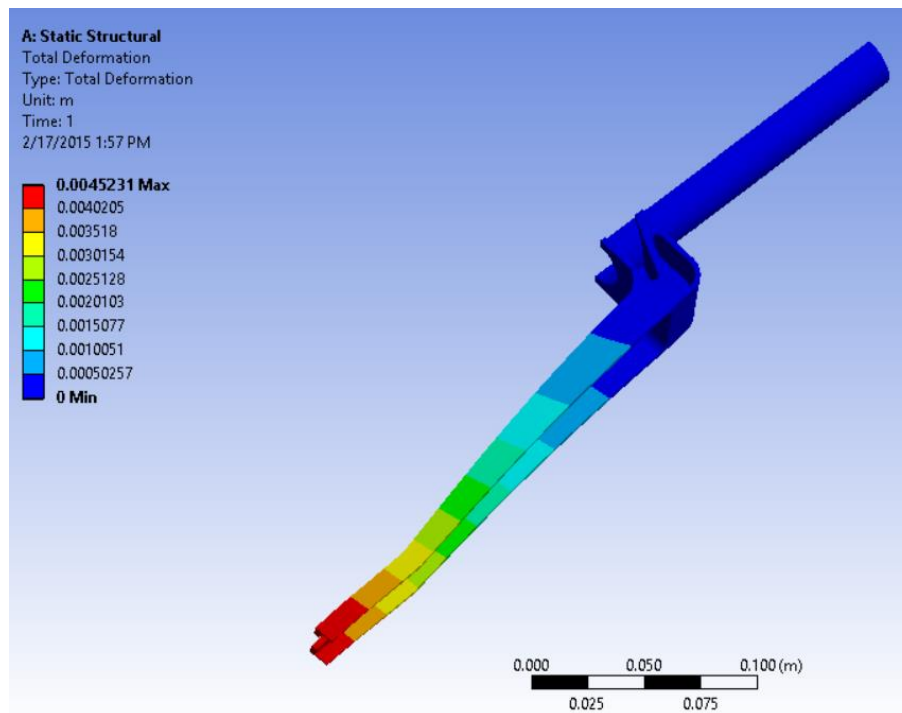


Figure 32. ANSYS Mechanical Axial Load Case Total Deformation

Appendix C

K.I.N.G.E.N.
(Kinetic Instrument to Navigate and
Gyroscopically Enforce Normality)

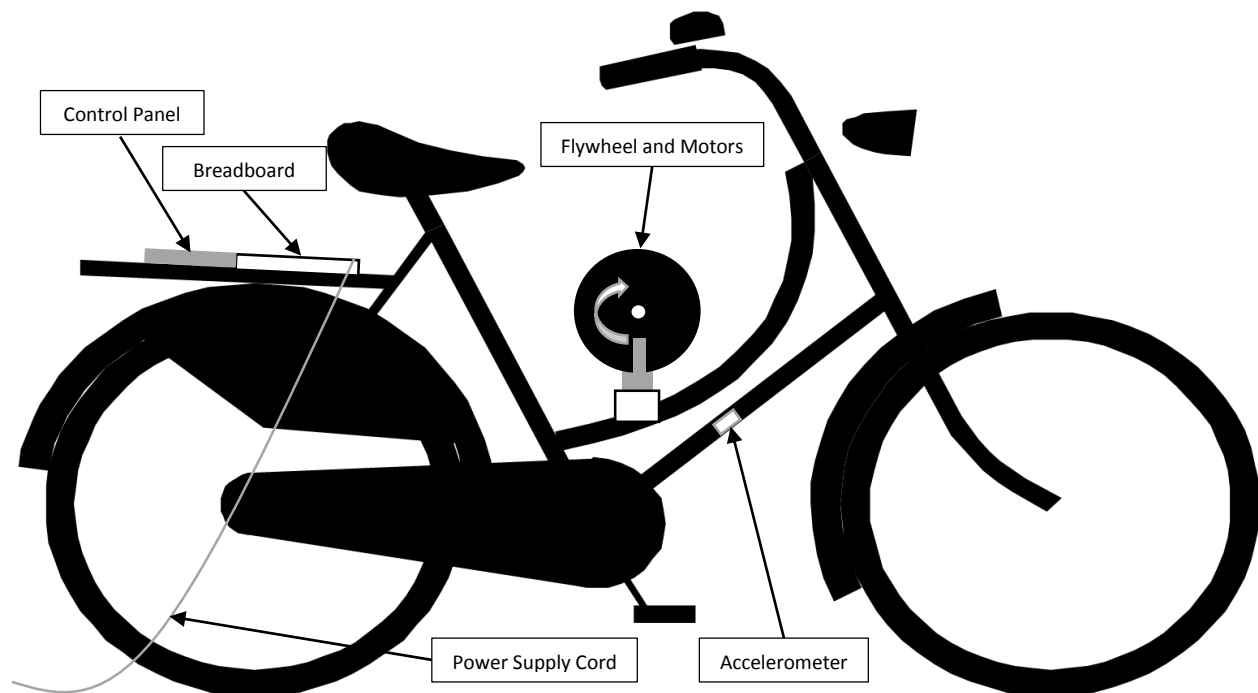
Melissa Murray & Ben Griffith

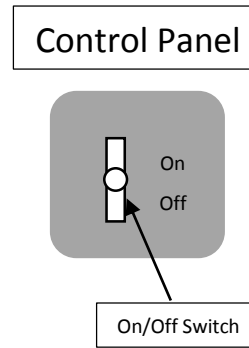
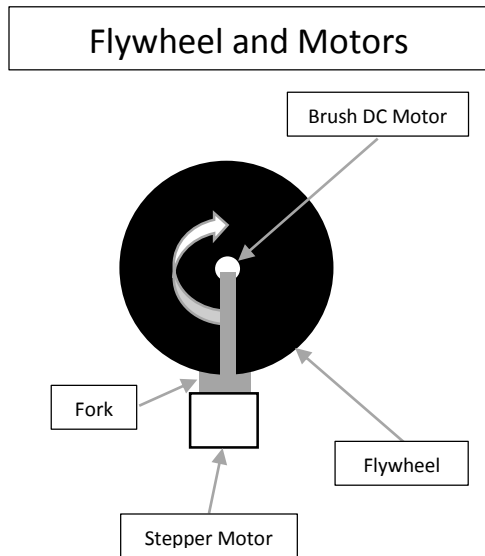
Description

We are members of the Human Powered Vehicle Team. We build a recumbent bike or trike with a fairing each year. When the vehicle is a bike, the rider has difficulty staying balanced when moving at slow speeds and when they are completely stopped. They are unable to put their feet on the ground to steady themselves because of the fairing. This problem causes them to fall often which could lead to minor injuries such as bruises. This problem also causes them to lose time in races. The goal of this project is to design a prototype gyroscopic system that will stabilize a model upright bike.

The gyroscopic system should be able to fit on a 12in tall upright bike along with its power supply and control panel. It should have a switch that allows the operator to turn it on and off as needed. If possible, it should stabilize the bike even when the bike is not moving. It will do this by taking input from an accelerometer and rotating a flywheel using a servo motors to counteract any leaning.

Sketch





Inputs to the μ Processor

- On/Off signal
- Bike lean

Outputs from the μ Processor

- Motor speed
- Flywheel rotational velocity
- Flywheel rotational angle

Parts Required

- Flywheel
- Stepper motor
- Breadboard + wires
- Power supply
- Brush DC motor
- Voltage regulator
- Mini Bike
- MOSFET
- H-Bridge
- Switch
- Metal rods
- Bearing
- Accelerometer

Goals

The minimum goal for this project is to make a system that can keep the bike up when stationary and rolling.

Extra

- Keep the bike upright when gently pushed
- Lean the bike to steer it
- Stand the bike up and balance it from a lying position on its side

Shopping List

Item	Supplier	Quantity	Price
NSD Spinner (Flywheel)	Amazon	2	\$40.00
12V Stepper Motor	Digi-Key	1	\$60.00+Shipping
Breadboard + Wires	ME Department	1	\$7.00
12V Power Supply	Amazon	1	\$50.00
12V Brush DC Motor	Digi-Key	1	\$100.00+Shipping
5V Regulator	ME Department	1	\$0.25
Our Generation Anywhere You Cruise Bicycle	Target	1	\$50.00+Shipping
MOSFET	Digi-Key	1	\$15.00+Shipping
H-Bridge	Robotics Team	1	\$50.00
Flip Switch	HPVT Spare Parts	1	\$0.00
Metal Rods	HPVT Scrap Metal	1 ft	\$0.00
Bearing	Fastenal	1	\$5.00+Shipping
Single Axis Accelerometer	Sparkfun	1	\$30.00+Shipping
TOTAL			~\$430

Appendix D

Determining the Effect of Bicycle Tire Pressure on Rolling Resistance

Final Design Report

20 February 2015

ME421-01

Dan Brindley

Ben Griffith

Crystal Hurtle

Melissa Murray

Table of Contents

1. Nomenclature	48
2. Introduction	49
3. Model and Derivation of Data Reduction Equation (DRE)	49
4. Measurands	50
5. Experimental Apparatus	51
6. Design	51
7. Procedure	53
8. Data	54
9. Results and Discussion	57
10. Conclusions	59
11. References	62
Appendix A – Bicycle Terminology	63
Appendix B – Sensor Systematic Uncertainty Information	65
Appendix C – Modifications to Experimental Procedure (Test and Refine)	66
Appendix D – Regression Method	67
Appendix E – Full DRE Derivation	1
Appendix F – MATLAB Curve Fitting and Uncertainty Code	3

Nomenclature

Term	Description	Units
$\frac{dV}{dt}$	total acceleration	$\frac{m}{s^2}$
A	frontal surface area	m^2
C_{rr}	coefficient of rolling resistance	-
C_d	drag coefficient	-
v_{bike}	velocity of bike (positive in the direction the bike is moving)	$\frac{m}{s}$
v_{wind}	velocity of wind (positive in the direction the bike is moving)	$\frac{m}{s}$
ρ	density of air	$\frac{kg}{m^3}$
g	acceleration due to gravity	$\frac{m}{s^2}$
m	mass of vehicle and rider	kg
$F_{rolling}$	force due to rolling resistance	N
F_{drag}	force due to aerodynamic drag	N
F_N	normal force from ground acting on bike tire	N
P	air pressure	Pa
R	individual gas constant of air	$\frac{J}{kgK}$

T	air temperature	K
---	-----------------	---

Introduction

The objective of the design was to determine the rolling resistance of a bicycle tire within 20% uncertainty and analyze the effect of tire pressure on rolling resistance. Rolling resistance is the total force that slows the spinning of the tire. Several factors contribute to rolling resistance, such as wheel deformation, bearing resistance, the load on wheel, wheel diameter, and riding surface conditions. Holding all other factors constant, an uncertainty of 20% allows us to inspect the effect of different tire pressures on rolling resistance. We determined the rolling resistance of the tire through coastdown testing, in which a faired recumbent bicycle (described in Appendix A) was accelerated and then allowed to coast down to a lower speed. The bicycle was provided by the Human Powered Vehicle Team. The data on rolling resistance will be of use to the team for determining the appropriate pressure to inflate the vehicle tires during competition.

There has been research done on the rolling resistance of bicycle tires. A coastdown testing procedure is outlined in the documentation of a 2013-14 ME421 project [1]. This procedure provided the basis for the procedure used in this experiment. In addition, SAE J1263 [2] and J2263 [3] outline coastdown testing procedures for automobiles, which we used as a starting point and adapted for bicycle testing.

Model and Derivation of Data Reduction Equation (DRE)

Figure 1 displays the forces acting on the bicycle while in motion.

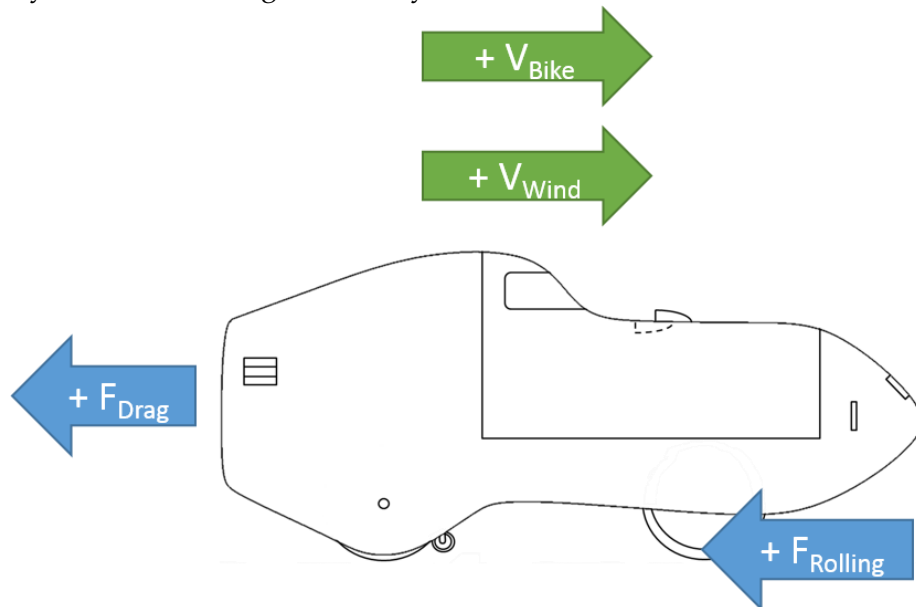


Figure 1: Free body diagram of bike. Velocities are with respect to the ground.

The DRE has first principles based in Conservation of Linear Momentum. The bicycle and rider are selected as a closed system. The corresponding equation is shown in (1).

$$\frac{dP_{sys}}{dt} = \sum F \quad (1)$$

From Figure 1, we see that the two forces acting on the bicycle are $F_{rolling}$ and F_{drag} . The force of rolling resistance is calculated in (2), and the force of wind resistance is calculated in (3), where $v_{bike} - v_{wind}$ represents air velocity when v_{wind} is a tailwind. The ground velocity data recorded by the bike computer will be adjusted using measured wind velocity data.

$$F_{rolling} = mgC_{rr} \quad (2)$$

$$F_{drag} = \frac{1}{2} C_d A \rho (v_{bike} - v_{wind})^2 \quad (3)$$

Additionally, the rate of change of linear momentum is described in (4).

$$\frac{dP_{sys}}{dt} = m \frac{dV}{dt} \quad (4)$$

Summing (2) and (3) to get the total force acting on the bicycle and substituting (4) for the change in linear momentum term results in an equation for C_{rr} . Putting this equation in terms of measurands using the ideal gas law, and rearranging to solve for C_{rr} results in (5), our DRE.

$$C_{rr} = -\frac{1}{2} \left(\frac{C_d A \left(\frac{P}{R T} \right) (v_{bike} - v_{wind})^2 + 2m \frac{dV}{dt}}{mg} \right) \quad (5)$$

Since (5) includes both velocity and acceleration, it is a differential equation, and we cannot solve for C_{rr} directly. However, we are able to fit the velocity data to a curve and pick out C_{rr} as a curve fit parameter. Thus, a rearranged version of (5) is shown below as (6). We solved (6) using a differential equation solver for velocity as a function of time with an initial condition of V_0 (in m/s), which represents the speed at the start of the coastdown segment, shown in (7). The full solution to the DRE is included as (10) in Appendix E.

$$\frac{dV}{dt} + \frac{C_d A P}{2RTm} V^2 = -gC_{rr} \quad (6)$$

$$(0) = V_0 \quad (7)$$

Measurands

Each variable in (6) was a measurand in the experiment with the exception of drag coefficient (C_d) and frontal area (A). These were grouped together to form a single variable (C_dA) that became a secondary parameter for the curve fitting. This method will be discussed in detail in a later section. The other measurands include bike velocity (v_{bike}), wind speed, (v_{wind}), air temperature (T), air pressure (P), and the mass of the bike and rider (m). To measure all of these variables, we selected sensors to reach our goal of 20% relative uncertainty in the resultant, C_{rr} .

Experimental Apparatus

The experimental apparatus included the 2012 Carnot Cycle, a faired recumbent bicycle from the Human Powered Vehicle Team, and a long stretch of flat pavement with enough space to get up to the determined speed and coast down in a straight line. We used the J1263 standards for automobile testing as a basis for selecting a testing site based on road surface and grade. The standards also require that the tests are run in each direction on the testing surface.

To calculate C_{rr} several things needed to be measured. A bike computer, which uses a magnetic sensor to detect each revolution of the wheel, is able to record the bike velocity versus time. A multi-function weather meter is able to measure the atmospheric conditions required for (6) – air pressure, air temperature, and wind speed. A scale is capable of measuring the mass of the bike and rider. The specifics of the instruments we selected are discussed in the Design section.

Design

In order to hit our target relative uncertainty of 20%, we needed to figure out how much uncertainty was acceptable in each measurand. To do this, we calculated uncertainty magnification factors (UMFs) using (8). For a representative value for velocity, we chose a single point that we expected to be towards the top of our velocity curve to represent the speed with the highest uncertainty.

$$UMF = \frac{x_i}{R} \frac{\partial C_{rr}}{\partial x_i} \quad (8)$$

In (8), x_i represents the representative value for each measurand, and R represents a representative value for the resultant, which is C_{rr} in our case. The UMFs were inserted into (9), shown below. Based on (9), we solved for what the acceptable relative uncertainty would be for each measurand if they were all the same.

$$\left(\frac{\omega_{C_{rr}}}{C}\right)^2 = (1.19)^2 \left(\frac{\omega_P}{P}\right)^2 + (1.19)^2 \left(\frac{\omega_T}{T}\right)^2 + (2.62)^2 \left(\frac{\omega_{v_{bike}}}{v_{bike}}\right)^2 + (0.23)^2 \left(\frac{\omega_{v_{wind}}}{v_{wind}}\right)^2$$

rr

$$+(1.19)^2 \left(\frac{\omega_m}{m}\right)^2 + (1.19)^2 \left(\frac{\omega_{C_dA}}{C_dA}\right)^2 + (1)^2 \left(\frac{\omega_{C_{rr,rand}}}{C_{rr,rand}}\right)^2 \quad (9)$$

This acceptable uncertainty for each measurand turned out to be approximately 5.6%. This gave us a starting point to look for sensors that met our requirements. The sensor we had the most difficult time finding was the wind sensor. Since the wind gauge had 11.2% relative uncertainty, we picked the rest of the sensors to be at or less than 5.6%. Having a low uncertainty in all of the sensors besides the wind gauge allowed us to decrease the allotted budget for these more certain sensors and increase the budget for the wind gauge. By this manipulation of the uncertainty budget, we were able to use the more uncertain wind speed sensor while still hitting our uncertainty target. The resulting relative uncertainties are summarized in Table 1.

Table 1: Uncertainty budget based on anticipated representative values

Measurand	Sensor	Repres. Value	Uncertainty	Uncertainty Capability	UPC
Drag Coefficient	---			5.6%	52.6%
Random	---			???	36.8%
Wind Speed	Kestrel 3500	1 m/s	0.11 m/s	11.2%	8.1%
Weight	Dymo S400	95 kg	0.91 kg	1.0%	1.5%
Bicycle Velocity	Garmin Edge 500	11.2 m/s	0.03 m/s	0.3%	<1.0%
Air Pressure	Kestrel 3500	101 kPa	0.15 kPa	0.1%	<1.0%
Air Temperature	Kestrel 3500	273 K	1.00 K	0.4%	<1.0%

To reach our uncertainty goal, some of the measurands were limited by their relative uncertainty, while other measurands were limited by their respective sensor. Based on the above uncertainty analysis, the bike must move faster than 0.71 m/s. Due to rider instability at low speeds, the lower bound had to be increased to 4.5 m/s to avoid parameters unaccounted for in our model such as wobble, slight turning, and feet dragging on the ground.

The anemometer (wind meter) is within our uncertainty budget regardless of the measured speed, so it is limited by the lower bound of the sensor itself. Under 0.3 m/s, the anemometer will not spin. The limits on the temperature sensor based on our uncertainty budget was

negative 249.2°C, but the valid operating range is -45°C to 125°C. Since we intend to be at least relatively comfortable during the testing, this will not be an issue. Similarly, the limit on air pressure based on uncertainty budget (at least 3.57 kPa) is not a concern, as the sensor's range is 30 kPa to 110 kPa, and the standard atmospheric pressure on Earth falls well within this range. In order to meet our uncertainty budget, our bike and rider system needed to have a mass of at least 22 kg. The bike itself has a mass of approximately 30 kg, so reaching this limit is not a concern.

Procedure

We tested with a set of Durano racing tires at three different pressures: 110 psi (758 kPa), 90 psi (620 kPa), and 70 psi (482 kPa). The highest pressure is the maximum inflation pressure recommended by the manufacturer, and the lowest pressure is the minimum tire pressure that allowed the bike to operate normally without risk of damaging the tire. We ran 12 trials per tire pressure, exceeding the 10 trials recommended by SAE J1263, checking the tire pressure and adjusting if necessary every six trials. The trials alternated direction on the course in order to reduce the effect of course slope (per SAE J1263).

We recorded the mass of the vehicle, which was the 2012 Carnot Cycle human powered vehicle, and all the participating riders, using the scale. We also measured the circumference of the inflated and mounted tires and used that circumference to set up the bike computer and sensor.

The testing site was a dry section of the Heritage Trail located behind Rose-Hulman Institute of Technology. Using GPS, we marked off the section of the course that met the grade specification. We had previously determined this location from a topographic map in conjunction with Google Earth.

Data collection began after a warm-up period of about 15 minutes. At the start of each set of trials for a given tire pressure, we checked the inflation pressure of the tires and adjusted it until it was at the targeted pressure.

The parallel wind velocity, crosswind velocity, atmospheric pressure, and air temperature were recorded with the weather meter at the beginning and end of each trial.

The rider began outside the testing zone and achieved the starting coastdown velocity of 25 mph (11.18 m/s) at the beginning of the zone. Upon reaching the coastdown zone, the rider stopped pedaling and coasted down to 10 mph (4.47 m/s) in a straight line. **Figure 1**Figure 2 illustrates the coastdown process.

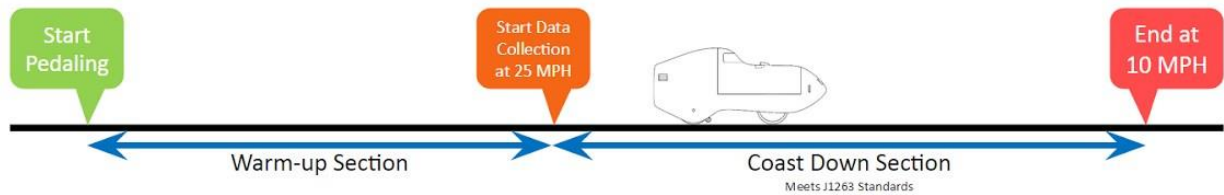


Figure 2: Coastdown testing procedure

Data

After all the data was collected, we downloaded the data from the bike computer and extracted the relevant sections. We truncated the velocity-time data to remove points recorded while the rider was still pedaling.

We then used a least-squares curve fitting function in MATLAB to fit our velocity-time model, (6), to the data by allowing the curve fitting tool to adjust the C_{rr} and C_dA parameters.

Total uncertainty in C_{rr} was determined through a regression technique that accounted for the uncertainty associated with the systematic uncertainty in the measurands (temperature, air pressure, and mass) within the velocity function. We simulated a normal distribution of 300 values for each measurand in the velocity function. In the normal distribution, the mean is equal to our nominal value for each measurand, and the standard deviation is equal to the systematic uncertainty for each measurand. We fit one least-squares curve for each of the 300 simulated sets of measurands. These 300 curve fits were combined into one representative curve fit for each trial.

We also considered the systematic uncertainty in velocity due to the capabilities of the bike computer. In our analysis, we tested different uncertainties for velocity ranging from sensationally small to laughably large. Despite a highly variable uncertainty in velocity, the total uncertainty in the curve fit remained unchanged, and this bothered us to our core. This is because the MATLAB function we used to curve fit the data tries to fit the data points as best it can, regardless of uncertainty in the data points. While we understand this is the case, it is clearly not optimal. Even though this problem bothers us, the several professors we consulted on the matter could not provide a better solution in our limited time frame. It remains a good candidate for future work.

We then accounted for random uncertainty between the trials at a specific tire pressure by comparing the value for C_{rr} against the trials at the same tire pressure. This method reports a total uncertainty for the curve fit parameter representing .

For more information on this regression technique, see Appendix D. See Appendix F for the MATLAB code written to perform this technique.

The velocity-time data of a single trial is shown in Figure 3 with its associated curve fit.

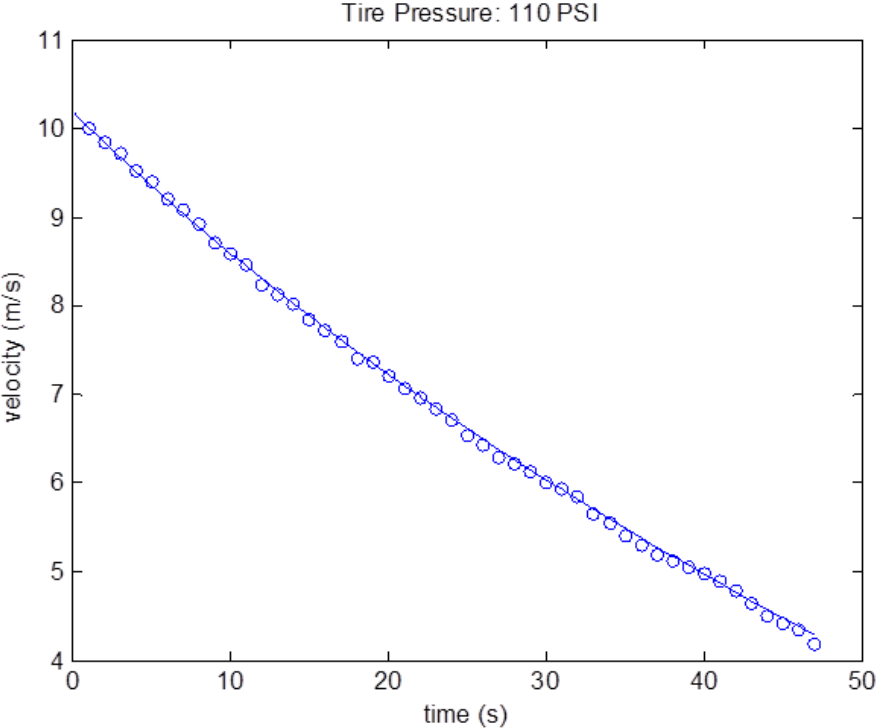


Figure 3: Sample velocity-time data for a single coastdown trial at 110 psi (758 kPa) and curve fit

Figure 4 shows six different curve fits for each of the six trials at 110 psi (758 kPa) in the same direction on the trail. The other two tire pressures showed a similar pattern.

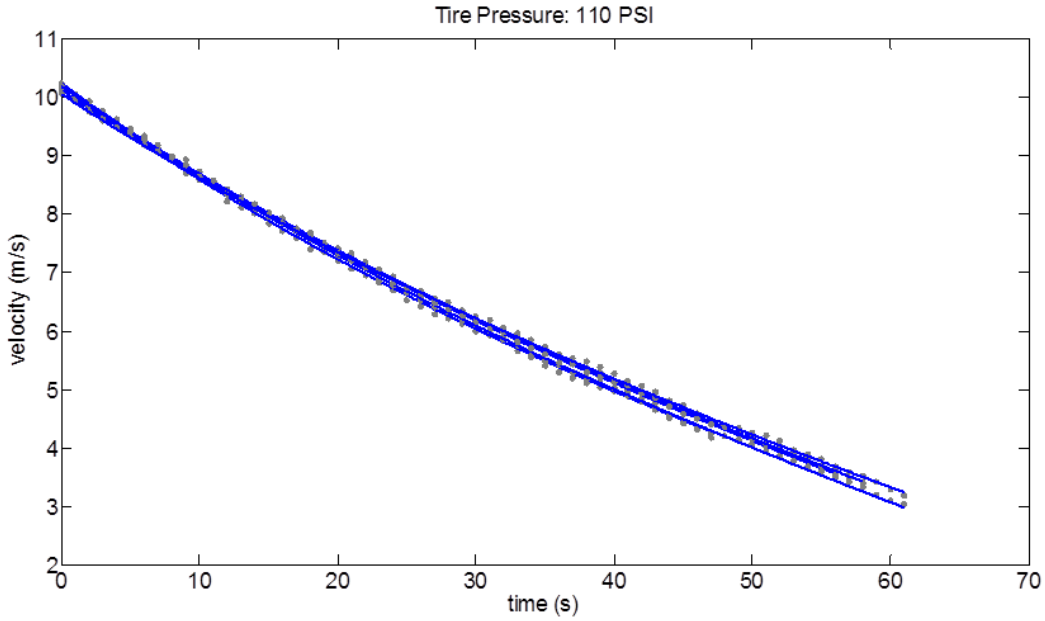


Figure 4: Six trials at the same tire pressure and direction with their associated curve fits

Next, we combined the C_{dA} and C_{rr} parameters for each of the six curve fits into a single curve fit that presents a C_{rr} representative of six trials at a single tire pressure in one direction on the trail. The representative curve fit for the eastbound trials for a 110 psi (758 kPa) tire pressure is shown below in Figure 5.

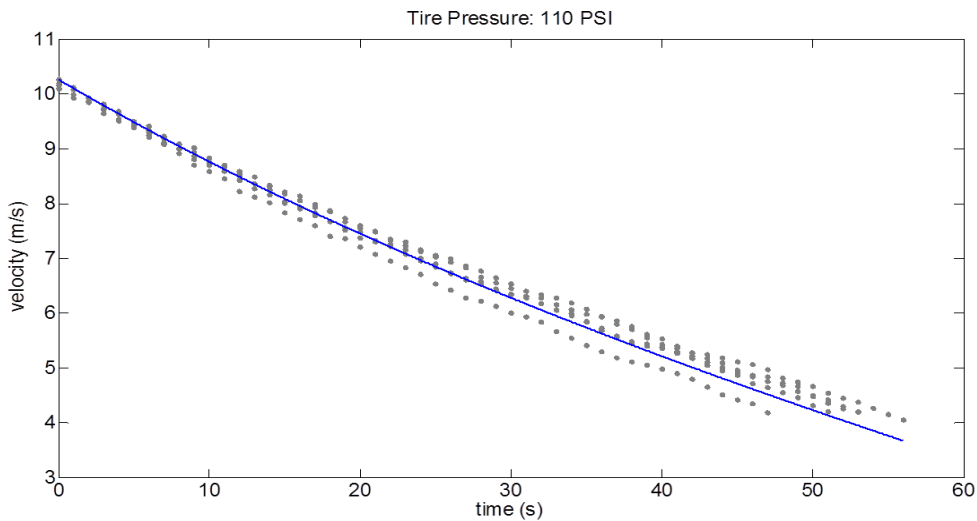


Figure 5: Final curve fit for eastbound 110 psi (758 kPa) data

It is worth noting that we did not simply combine all the data for a single tire pressure in one direction and fit one curve fit. Such a technique would not account for changes in temperature, air pressure, or mass, each of which varied between the six trials in the data set.

In the model we fit to the data, whenever C_{dA} appeared, C_{rr} appeared multiplied by it, but C_{dA} also appeared elsewhere on its own. This meant that the curve fitting algorithm could have fit the C_{dA} parameter first since C_{rr} appeared to be dependent on it. Since C_{rr} was what we truly cared about, we decoupled C_{dA} and C_{rr} so the algorithm would fit them with equal weight. To do this, we replaced each $C_{rr} * C_{dA}$ combination with a single variable $C_{rr}C_{dA}$. After the algorithm fit both C_{dA} and $C_{rr}C_{dA}$, we divided $C_{rr}C_{dA}$ by C_{dA} and thus calculated the C_{rr} parameter. This did not appear to affect the overall result, so we left the two parameters separate for our final analysis.

Also, to determine what variations our curve fitting algorithm was most sensitive to, we looked at the Jacobian matrices resulting from the curve fit. This tells us which parameters our curve fitting algorithm focused on changing and which it changed less. If, for example, the algorithm focused on C_{dA} instead of C_{rr} , we would have less confidence in the C_{rr} parameter. Thankfully this was not the case, as the Jacobian for C_{rr} outweighed that of C_{dA} .

Results and Discussion

Using this experimental set up, the coefficient of rolling resistance of Durano bicycle tires on a recumbent faired bicycle at three different inflation pressures was determined with 30% uncertainty, which is greater than our initial goal of 20%.

Due to this large uncertainty, each of the three values of rolling resistance for different tire pressures fell within the uncertainty range of the other values. This can be seen in Figure 6. These overlapping values kept us from differentiating between tire pressures and ultimately made our results inconclusive.

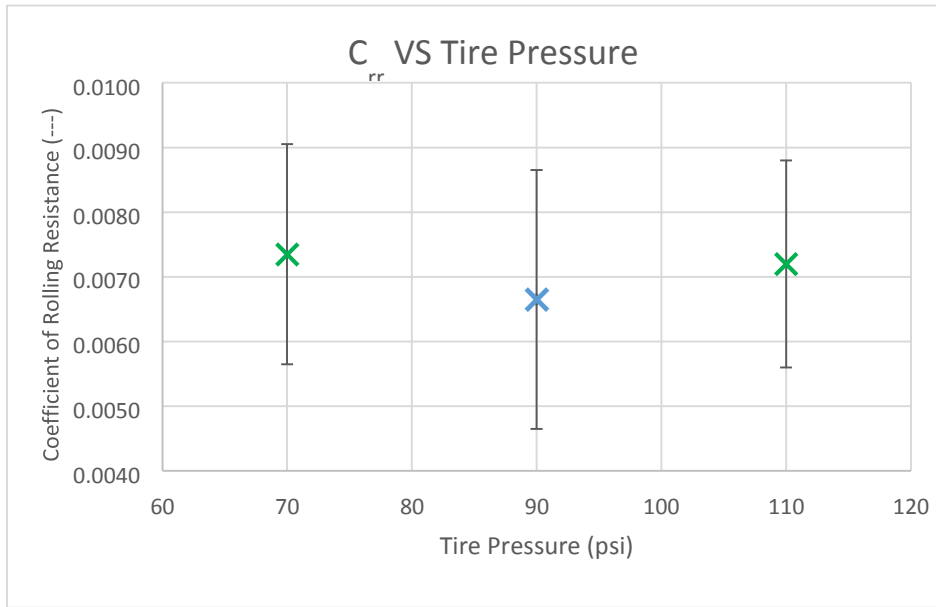


Figure 6: C_{rr} VS Tire Pressure shows overlapping uncertainty ranges

We determined that either the testing procedure needed to be modified to reach a lower uncertainty, or our model of the system needed to be modified to account for slope in the testing area. One of the possible modifications to the procedure was increasing the number of trials to reduce the random uncertainty which dominated the total uncertainty. The number of trials required to reduce the random uncertainty to 5.6%, per our original budget, would be approximately 330. Due to time constraints, we were not able to implement either a change in the procedure or a change in the model.

The grade in the testing area, though just 1%, proved to be a large enough factor that the east- and westbound trials provided noticeably different coefficients of rolling resistance. The trials in each direction were similar enough to each other that the random uncertainty made up a lower portion of the total uncertainty. When we split the trials up into eastbound and westbound, the uncertainty dropped low enough to enter our desired range, as shown in Table 2.

Table 2: Uncertainty table summarizing testing results

Direction	Average C_{rr}	Total Uncertainty	C_{rr} Systematic Uncertainty	Random Uncertainty	Relative Uncertainty
W	0.0061	0.000736	7.06E-04	2.50E-06	12.1%
E	0.0083	0.000247	1.18E-04	2.17E-04	3.0%

W	0.0065	0.0012	1.20E-03	7.27E-06	18.5%
E	0.0082	0.0012	1.20E-03	7.16E-06	14.6%
W	0.0053	0.000458	3.90E-04	7.60E-07	8.6%
E	0.0080	0.000735	7.25E-04	2.63E-06	9.2%

Despite this drop in uncertainty to an average of approximately 11%, each of the three values in each direction overlapped as seen in Figure 7, meaning our data was still inconclusive.

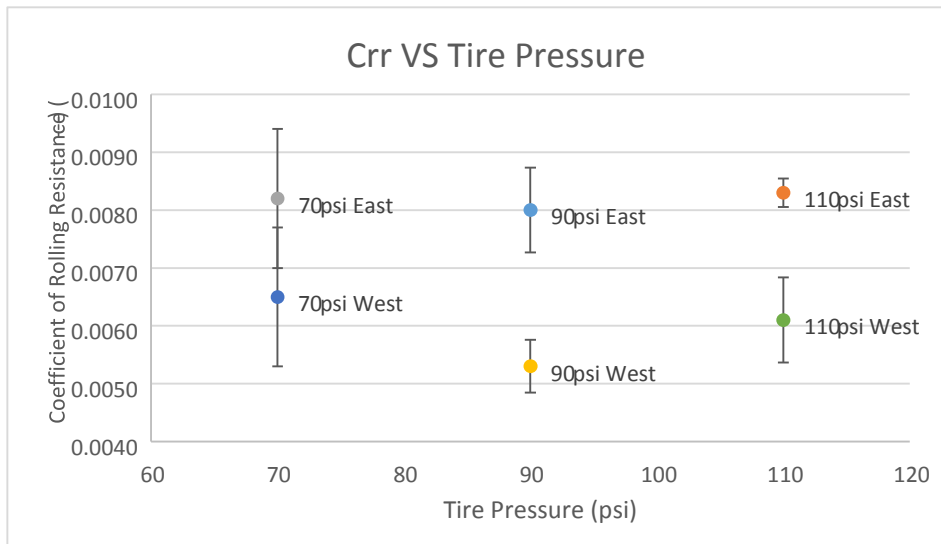


Figure 7: C_{rr} VS Tire Pressure split into east and west-bound trials significantly reduces random uncertainty

The C_dA also changed with trial direction, varying as much as 40%. This is most likely because the model, which didn't account for a grade, attempted to account for the change in grade by varying the parameters it had access to, most notably, C_dA . This being said, the C_dA values are close to the values we expected. The C_dA calculated from a previous ME421 team for a different bicycle was 0.066 [1]. Since our bicycle was of a similar shape and a larger size, we expected our C_dA to be larger. This proved to be the case, as our smallest C_dA was calculated to be 0.069.

Conclusions

In conclusion, we did not reach our project goal of being able to determine the effect of bicycle tire pressure on rolling resistance. We did not meet our uncertainty goal of 20%, and we are unable to distinguish a meaningful difference in the coefficient of rolling resistance between tire pressures of 110 psi (758 kPa), 90 psi (620 kPa), and 70 psi (482 kPa). Prior art indicated that a similar range of tire pressures should produce a range of rolling resistance coefficients each separated by at least 20%. In our experiment, we could have further separated the tire pressures to differentiate between them, but they would have been so far apart that they would have been unusable on a bicycle due to dangerous operating conditions. Therefore, we need to refine the experiment instead of changing the tire pressures.

The coefficient of rolling resistance of the tires did fall within the range specified by the manufacturer, Schwalbe. They stated the tires should have a coefficient of about 0.0061 when inflated to a pressure of 116 psi (800 kPa). At 110 psi (760 kPa) we calculated the coefficient of rolling resistance to be 0.0072 ± 0.0016 .

The SAE papers “The determination of vehicle drag contributions from coast-down tests” [4] and “Tire Rolling Resistance Measurements from Coast-down Test” [5] confirm that the design procedure we employed was adequate for determining rolling resistance in a tire.

Nevertheless, there are a few aspects of this experiment that could be changed to improve the quality of the results. While we followed the standards outlined in SAE J1263 [2] and J2263 [3], we were unable to meet the minimum recommended temperature. Due to time constraints, we could not wait for weather that met the temperature requirement and therefore conducted our trials at a temperature below the temperature range recommended by the standards.

Additionally, while the grade of the test course met these standards, it could still be improved. As mentioned in Appendix C, the location of testing was changed from the Terre Haute International Airport to the Heritage Trail. The Terre Haute International Airport however, would have been a better test course because it has a lower grade (about 0.07% grade at the airport compared with about 1% grade on the Heritage Trail), which would reduce the effects of slope on the resultant.

If the refinements are not adequate, there is an alternative method we could employ. Wheel Energy, an independent testing lab in Finland that has contracts with major bike manufacturers like Trek and Specialized, uses a power transfer test with a steel drum. Essentially, the wheel is mounted on an arm above a steel drum so that it rolls on the powered drum's surface, as shown in Figure 8. A downward force is applied to the wheel to simulate loading from the bike, and the steel drum is accelerated to a constant velocity. By measuring the power transfer between the drum and the wheel, the coefficient of rolling resistance can be calculated. Because C_{rr} is dependent on road surface, these values won't necessarily be the same as those we found on the road, but they would be useful for comparing different inflation pressures in a more easily controlled environment.



Figure 8: Power transfer test with steel drum

Finally, while we thoroughly developed our regression method, even further development could improve the quality of our results. This would involve additional study in the field of regression and advanced statistics.

References

- [1] J. Anderson *et al*, "Coast-Down Testing of a Rose-Hulman Human Powered Vehicle," unpublished.
- [2] Road Load Measurement and Dynamometer Simulation Using Coastdown Techniques, SAE J1263, March 9, 2010.
- [3] Road Load Measurement Using Onboard Anemometry and Coastdown Techniques, SAE J2263, December 12, 2008.
- [4] R. White *et al*, "The determination of vehicle drag contributions form coast-down tests," SAE Technical Paper Series, vol. 72009, pp. 1-12, Jan. 1972.
- [5] B. Dayman, "Tire rolling resistance measurements from coast-down tests," SAE Technical Paper Series, vol. 760153, pp. 354-359, Feb. 1976.
- [6] Eric Reyes, private communication, Feb. 2015.

Appendix A - Bicycle Terminology

Upright Bike

An upright bike is the most common type of bicycle in which the rider sits with their legs under them. A picture of a basic upright bike is shown in Figure 1, below.

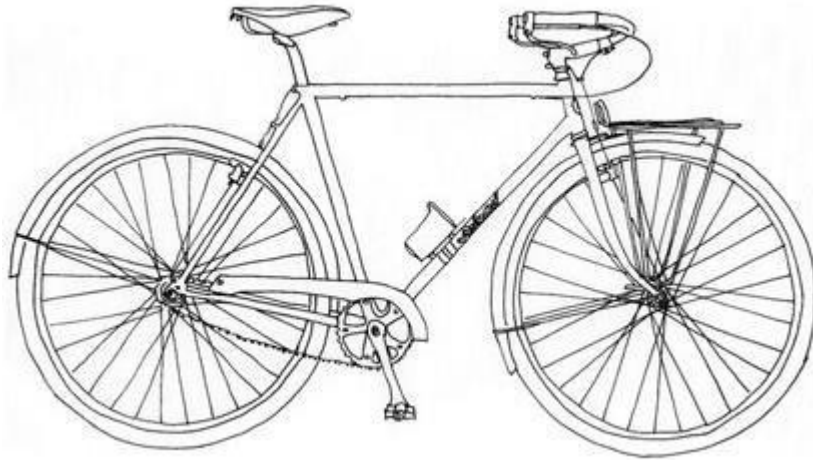


Figure 1: Upright bicycle

Source: <http://belovedcycles.com/wp-content/uploads/morton-2011-new-drawing.jpg>

Recumbent Bike

A recumbent bike is a bike in which the rider is in a reclined position with their legs in front of them. Recumbent bikes have an advantage to upright bikes in that they allow the rider to exert more power and have a smaller, more aerodynamic profile. A picture of a basic recumbent bike is shown in Figure 2 below.

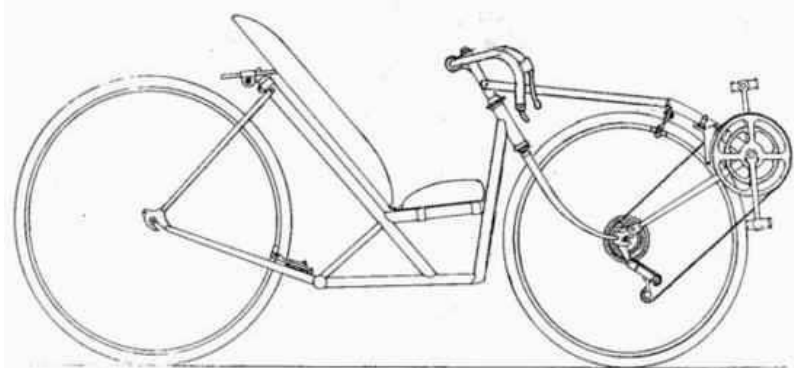


Figure 2: A recumbent bike

Source: <http://users.skynet.be/ligfiets/phC3/bikeplans.jpg>

Fairing

A fairing is an external shell placed around a vehicle to reduce aerodynamic drag. While common on cars and motorcycles, they are also advantageous for bicycles. Figure 3 shows a recumbent bike with a fairing as well as a transparent view of the bike with the top part of the fairing removed. A tiller, labeled in this figure, is the equivalent of handlebars and is used for steering the bike. Figure 4 is a picture of the 2012 Carnot Cycle used for this experiment.

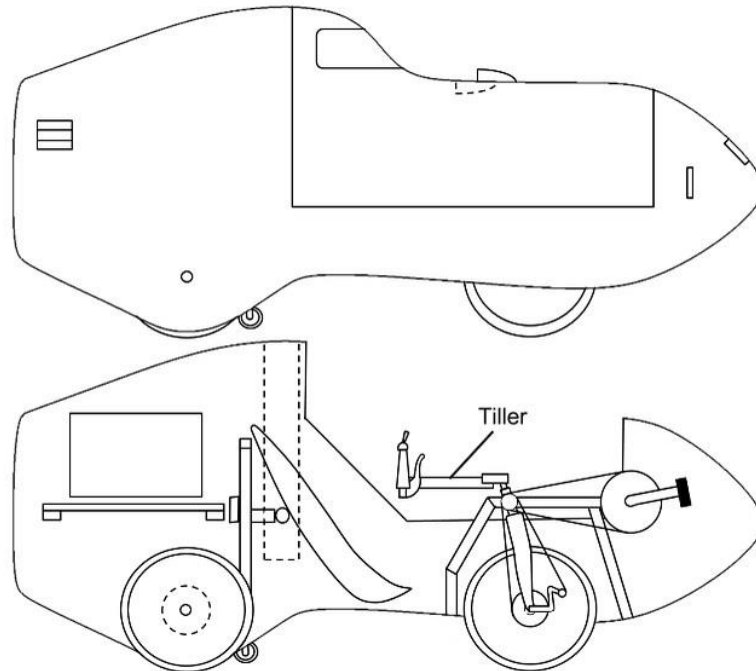


Figure 3: A faired recumbent bicycle.



Figure 4: The 2012 Carnot Cycle.

Appendix B - Sensor Systematic Uncertainty Information

Sensor Name	Source	Units	Min Value	Max Value	Resolution	Accuracy	Expected Value	Systematic Uncertainty				Total Syst Uncert (metric units)
								Accuracy	Readability	Total Syst Uncertainty	Readability	
Garmin Edge 500	Dept	m/s	?	?	0.003175 (m)	1 (mm)	5 to 15	2.24E-02	2.24E-02	0.0316	0.0316 (m/s)	
Kestrel 3500	Dept	m/s	0.4	60	0.1	Larger of 3% or least significant digit	1.0	0.1	0.05	0.1118	0.1118 (m/s)	
Kestrel 3500	Dept	hPa	300	1100	0.1	1.5	1010	1.5	0.05	1.5008	150.0833 (Pa)	
Kestrel 3500	Dept	°C	-29	70	0.1	1	0	1	0.05	1.0012	1.0012 (°C)	
Dymo S400	Dept	kg	1	181	0.2	+/-1 lb under 110lb, +/-2 lb over 110lb	95	0.907	0.1	0.9125	0.9125 (kg)	
Topeak D2	HPVT	psi	0	250	1	Not given, assume same as resolution	10 to 120	0.5	0.5	0.7071	4875.3296 (Pa)	

Appendix C - Modifications to Experimental Procedure (Test and Refine)

A significant change to our procedure was to conduct testing on the Heritage Trail rather than at the Terre Haute International Airport. The airport was unable to provide an area for testing due to a schedule conflict, so we found the straightest and flattest section of the Heritage Trail, which is located between the Rose-Hulman SRC and the end of the football field. The slope at this location is just at the edge of what is acceptable by SAE standards, but by doing runs in both directions, we are mitigating the effect of slope on our results, a method that is supported by the SAE standards for the same reason. For future testing with a longer timetable, we'd schedule time at the Terre Haute airport in order to further reduce the effect of slope on our results.

Another change to testing was the testing platform. During our shakedown, we planned on using a three wheeled human powered vehicle (the Namazu), but the vehicle was damaged during the warmup period. Due to time constraints, we used an upright road bike for shakedown testing, but for the final testing, we switched to a two wheeled vehicle (the Carnot Cycle). We outfitted it with the same new Durano tires that we were planning to use on the three-wheeled vehicle.

One more change to the procedure was the use of multiple riders. This ensured that each rider was able to reach the starting speed of 25 mph (11.18 m/s) for the trial and could switch out when they became fatigued. Because the rider's only purpose is to get the bike up to speed, the only difference they make during the coasting portion is their contribution to the mass of the bike. We recorded the weight of each rider with the bike before the testing, and then recorded which rider was in the vehicle during each trial. During the data analysis, we used the corresponding mass of rider and bike for the curve fitting process on each trial.

A future possible change to the procedure would be to measure the circumference of the wheel with a rider in the bike. The added weight of the rider would compress the wheel and slightly decrease the circumference. In addition to this, the circumference should be measured with each rider at each tire pressure to ensure accurate velocity data.

Appendix D - Regression Method

Since our desired parameters resulted from curve fitting our data, we needed to utilize a method of calculating uncertainty that allowed us to report a value of total uncertainty in the curve fit.

The uncertainty in C_{rr} is calculated through use of the Jacobian matrix and residuals resulting from the least squares curve fit. Using (1) provides the uncertainty in C_{rr} and C_{dA} .

$$\begin{matrix} \sigma_{C_{dA}}^2 & X \\ X & \sigma_{C_{rr,sim}}^2 \end{matrix} = \left(\frac{1}{N-1} \sum_{i=1}^N r_i^2 \right) [J^T J]^{-1} \quad (1)$$

In this equation, N is the number of data points, r_i is the residual from each curve fit, and J is the Jacobian matrix related to each trial. This equation calculates the uncertainty in rolling resistance in one trial due to uncertainty in velocity alone.

Each of our measurands -- temperature, pressure, and mass -- has its own systematic uncertainty related to the chosen sensor capabilities. To account for this systematic uncertainty, we simulated 300 temperatures, pressures, and masses over a normal distribution where the mean of each distribution was our measured value and the standard deviation was the systematic uncertainty we calculated from the sensor data sheets. For each set of measurands, we ran a least squares curve fit. Each of these curve fits using the simulated measurands were averaged together to provide a representative value of C_{rr} . To account for this uncertainty in the simulated measurands as well as the uncertainty in velocity we use (2).

$$\sigma_{C_{rr,sim,tot}}^2 = \frac{1}{m} \sum_{i=1}^m \sigma_i^2 + \frac{1}{m-1} \sum_{i=1}^m \left(C_{rr,i} - \frac{1}{m} \sum_{i=1}^m C_{rr,i} \right)^2 \quad (2)$$

In this equation, m is the number of simulated trials, σ_i^2 is the uncertainty calculated from (1), and $C_{rr,i}$ is the calculated rolling resistance from each simulated trial. Equation (2) results in the total systematic uncertainty in rolling resistance. To come up with a single value for C_{rr} , we averaged each value corresponding to the same tire pressure. We then accounted for the random uncertainty between trials with (3).

$$\begin{aligned} & \frac{\sum_k (C_{rr,i} - C_{rr,avg})^2}{k-1} = \sum_{i=1}^{k-1} \sigma_{C_{rr,i}}^2 + \frac{1}{k-1} \end{aligned} \quad (3)$$

where k represents the number of trials being considered, $C_{rr,i}$ is the value calculated for each trial and $C_{rr,avg}$ is the average value among the trials being considered. This equation was used to calculate a single C_{rr} for each tire pressure and the total uncertainty associated with that C_{rr} . In order to test this algorithm, we used different uncertainties for velocity ranging from sensationally small to laughably large. Despite a highly variable uncertainty in velocity, the total uncertainty in the curve fit remained unchanged, and this bothered us to our core. This is because the MATLAB function we used to curve fit the data tries to fit the data points as best it can, regardless of uncertainty in the data points. While we understand this is the case, it is clearly not optimal. Even though this problem bothers us, the several professors we consulted on the matter could not provide a better solution in our limited time frame. If this project was to be pursued in the future, a more comprehensive uncertainty analysis would be required. [5]

Appendix E – Full DRE Derivation

The DRE has first principles based in Conservation of Linear Momentum. The equation corresponding to this is shown in (1).

$$(1) \quad \frac{dP_{sys}}{dt} = \Sigma F$$

$$F_{rolling} = g m C_{rr} \quad (2)$$

$$F_{drag} = \frac{1}{2} C_d A \rho (v_{bike} - v_{wind})^2 \quad (3)$$

$$\frac{dP_{sys}}{dt} = ma \quad (4)$$

Combine (1), (2), (3), and (4).

$$ma = -F_{rolling} - F_{drag} \quad (5)$$

Putting this in terms of measurands turns (5) into (6).

$$(6) \quad m g C_{rr} + \frac{(v_{bike} - v_{wind})^2 ((C_d A) \rho)}{2} = m a$$

Since we cannot measure air density directly, we must use the ideal gas equation to calculate it. This is shown in (7).

$$P V = m R T \quad (7)$$

Rearranging (7) into a useful form results in (8).

$$\rho = \frac{P}{R T} \quad (8)$$

Substituting (8) into (6) results in (9).

$$(8) \quad m g C_{rr} + \frac{(v_{bike} - v_{wind})^2 ((C_d A) \frac{P}{R T})}{2} = m a$$

Rearranging to find C_{rr} leads to (9), our DRE.

$$C_{rr} = -\frac{1}{2} \left(\frac{C_d A \left(\frac{P}{RT} \right) (v_{bike} - v_{wind})^2 + 2am}{mg} \right) \quad (9)$$

Equation (9) is a differential equation, so we cannot solve for C_{rr} directly. However, we are able to fit the velocity data to a curve and pick out the C_{rr} as a coefficient of the curve fit. Thus a differential equation solver was used to solve (9) for velocity as a function of time, shown in (10).

$$v(t) = \frac{\sqrt{2C_d A P m g C_{rr} R T}}{C_d A P} \tan \left(\frac{\sqrt{2}}{2RTm} \left(\sqrt{2RTm} \tan^{-1} \left(\frac{V_0 C_d A P}{\sqrt{2C_d A P m g C_{rr} R T}} \right) - t \sqrt{C_d A P m g C_{rr} R T} \right) \right) \quad (10)$$

Appendix F – MATLAB Curve Fitting and Uncertainty Code

```
%{
trialAverager
Description: Top level code which reads in the data files,
passes the data to a curve fitting function and writes the
results to an excel file

Authors: Daniel Brindley & Crystal Hurtle
Last modified: 2/19/2015
%}
%%
    clc
clear all
close all

%reads in raw excel files MAKE FILENAMES THE SAME LENGTH
filename1 = {'Trial1.xlsx ','Trial3.xlsx ','Trial5.xlsx
','Trial7.xlsx ','Trial11.xlsx'};
filename2 = {'Trial2.xlsx ','Trial4.xlsx ','Trial6.xlsx
','Trial8.xlsx ','Trial10.xlsx','Trial12.xlsx'}; filename3
=
{'Trial13.xlsx','Trial15.xlsx','Trial17.xlsx','Trial19.xlsx','Tr
ial21.xlsx','Trial23.xlsx'}; filename4 =
{'Trial14.xlsx','Trial16.xlsx','Trial18.xlsx','Trial20.xlsx','Tr
ial22.xlsx','Trial24.xlsx'}; filename5 =
{'Trial25.xlsx','Trial27.xlsx','Trial29.xlsx','Trial31.xlsx','Tr
ial33.xlsx','Trial35.xlsx'}; filename6 =
{'Trial26.xlsx','Trial28.xlsx','Trial30.xlsx','Trial32.xlsx','Tr
ial34.xlsx','Trial36.xlsx'};

filenames = {filename1, filename2, filename3, filename4,
filename5, filename6};

for k = 1:length(filenames)
    %Sets the current data set to be analyzed
    filename = cellstr(filenames{k});      results
= zeros(length(filename),3);

        for i = 1:length(filename)%runs the curve fit for each
specified trial
            [results(i,1),results(i,2),results(i,3), speed, time] =
curveFitDan(filename{i});
            xlswrite('Results', speed, i, 'A');
        xlswrite('Results', time, i, 'B');
```

```

        %reported value for Crr
CrrAvg = mean(results(:,1));
xlswrite('Results', CrrAvg, i, 'D');
CdaAvg = mean(results(:,3));
xlswrite('Results', CdaAvg, i, 'E');

        %the mean of the squared systematic uncertainty in Crr
Crr_sys_unc2 = mean(results(:,2).^2);

        %calculates the random uncertainty (scatter between
        trials)
        rand = 0;
        num_trials = length(filename);
for j = 1:num_trials
        rand = rand + (results(j,1) - CrrAvg)^2;
end
        varCrr = 1/(num_trials-1)*rand;

        total_unc2 = Crr_sys_unc2 + varCrr; %Total squared
        uncertainty

        %total uncertainty for the whole thing
total_unc = sqrt(total_unc2);
        xlswrite('Results', total_unc, i, 'F');
end end

%{ curveFit
Description: Lower level function that takes in data from a
single trial, simulates the measurands to account for systematic
uncertainty and generates a best fit curve to the data.

Parameters: filename      - excel sheet containing data to
be analyzed

Outputs:
CrrAvg      - average Crr across all simulated trials
total_unc   - total systematic uncertainty due to uncertainty in measurands
CdAAvg      - average CdA across all simulated trials
Authors: Daniel Brindley & Crystal Hurtle
Last modified: 2/19/2015
%}

```

```

function [CrrAvg,total_unc,CdAAvg] = curveFitDan(filename)
%% READ IN DATA

truncationSpeed = 10.28; % m/s
time = xlsread(filename, 'Sheet1', 'A:A').*(3600*24);
speed = xlsread(filename, 'Sheet1', 'C:C'); weather_data
= xlsread(filename, 'Sheet2');
[~, eastOrWest,~] = xlsread(filename,'Sheet2','G2'); %reads in
the direction of the trial

% modify the speed based on windspeed and direction
if strcmp(eastOrWest,'E')      speed = speed -
weather_data(2); else
    speed = speed + weather_data(2); end

%% Truncate data to ~ 23 mph/10.28mps z
= 1;
while speed(z) > truncationSpeed
z = z+1; end
speed = speed(z:end); time
= time(z:end);

time = time - min(time); %sets the first time point to zero

%% SIMULATE TRIALS

%number of simulations
N = 5;
nom_temp = weather_data(4) + 273; %Kelvin temp_unc
= 1.0012; %Kelvin

nom_pres = weather_data(5)*100; %Pa pres_unc
= 150.0833; %Pa

nom_mass = weather_data(6); %kg mass_unc
= .9125; %kg

% Generate normal distributions based on uncertainty in
measurements
pd_T = makedist('Normal','mu',nom_temp,'sigma',temp_unc); pd_P
= makedist('Normal','mu',nom_pres,'sigma',pres_unc); pd_m =
makedist('Normal','mu',nom_mass,'sigma',mass_unc);

```

```

    for
    i=1:1:N
        temps(i,1) = random(pd_T);
        pressures(i,1) = random(pd_P);
        masses(i,1) = random(pd_m); end

%%%%%%%%%%%%%%%%%%%%%%%%%%%%%%%%%%%%%%%%%%%%%%%%%%%%%%%%%%%%%%%%%%%%%%%%
%%%%%%%% WEIGHT VELOCITY %%%%%%%%%
%%%%%%%%%%%%%%%%%%%%%%%%%%%%%%%%%%%%%%%%%%%%%%%%%%%%%%%%%%%%%%%%%%%%%%%%

% Velocity uncertainty velo_unc2
= .2;

v_weighted = sqrt(1/velo_unc2).*speed;

%% PERFORM CURVE FIT

%parameters for lsq curve fit
guess = [.1,.009]; lb =
[0,0]; ub = [2,0.1];

%define constants R
= 286.9; %J/(kg*K) g
= 9.81; %m/s^2
V0 = speed(1); %m/s

for i = 1:1:N
    %weighted model function - solution to the differential
equation    model_fcn =
@(b,time) (sqrt(1/velo_unc2))*(1/(b(1)*pressures(i)))*(tan(.5*(R*
temps(i)*masses(i)*sqrt(2)*atan((V0/2)*b(1)*pressures(i)*sqrt(2)
/sqrt(b(1)*pressures(i)*g*masses(i)*b(2)*R*temps(i))))time.*sqrt(
b(1)*pressures(i)*g*masses(i)*b(2)*R*temps(i)))*sqrt(
2)/(R*temps(i)*masses(i))*sqrt(b(1)*pressures(i)*g*masses(i)*b(
2)*R*temps(i))*sqrt(2));
    %run the least squares curve fit
    [mdl(:,i),~,residual(:, i),~,~,~,jacob(:,2*i-1:2*i)] =
lsqcurvefit(model_fcn,guess,time,v_weighted,lb,ub); end

%convert jacobian to a normal matrix jacob
= full(jacob);

Crr = mdl(2,:);
CrrAvg = (1/N)*sum(mdl(2,:));
CdAAvg = (1/N)*sum(mdl(1,:));

```

```

%% CALCULATE UNCERTAINTY
for
i=1:1:N
    Rs(:,2*i-1:2*i) = (1/(size(speed,1) -
2))*sum(residual(:,i).^2).*inv(jacob(:,2*i-1:2*i)'*jacob(:,2*i-
1:2*i));
    sigmaCrr2(i) = Rs(2,2*i); end

total_unc = (1/N)*sum(sigmaCrr2)+1/(N-1)*sum(Crr - CrrAvg)^2;
total_unc = sqrt(total_unc);

%% PLOT DATA AND RESULTS

t = 0:.01:time(end);
curve_fit
=(1/(mdl(1)*pressures(i)))*(tan(.5*(R*temps(i)*masses(i)*sqrt(2)
*atan((V0/2)*mdl(1)*pressures(i)*sqrt(2)/sqrt(mdl(1)*pressures(i)
)*g*masses(i)*mdl(2)*R*temps(i)))-
t.*sqrt(mdl(1)*pressures(i)*g*masses(i)*mdl(2)*R*temps(i)))*sqrt
(2)/(R*temps(i)*masses(i))*sqrt(mdl(1)*pressures(i)*g*masses(i)
*mdl(2)*R*temps(i))*sqrt(2));

plot(time,speed,'o')
title('Tire Pressure: 110 PSI')
xlabel('time (s)')
ylabel('velocity (m/s)') hold
on plot(t,curve_fit) hold off
end

```